
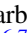



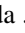
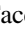


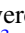
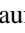
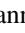


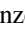




# xCOLD GASS: The Complete IRAM 30 m Legacy Survey of Molecular Gas for Galaxy Evolution Studies

Amélie Saintonge<sup>1</sup> , Barbara Catinella<sup>2</sup> , Linda J. Tacconi<sup>3</sup> , Guinevere Kauffmann<sup>4</sup>, Reinhard Genzel<sup>3</sup> , Luca Cortese<sup>2</sup> ,  
Romeel Davé<sup>5,6,7</sup>, Thomas J. Fletcher<sup>1</sup> , Javier Graciá-Carpio<sup>3</sup>, Carsten Kramer<sup>8</sup>, Timothy M. Heckman<sup>9</sup> ,  
Steven Janowiecki<sup>2</sup> , Katharina Lutz<sup>10</sup> , David Rosario<sup>11</sup> , David Schiminovich<sup>12</sup>, Karl Schuster<sup>13</sup>, Jing Wang<sup>14</sup> ,  
Stijn Wuyts<sup>15</sup> , Sanchayeeta Borthakur<sup>16</sup> , Isabella Lamperti<sup>1</sup> , and Guido W. Roberts-Borsani<sup>1</sup> 

<sup>1</sup> University College London, Gower Street, London WC1E 6BT, UK

<sup>2</sup> ICRAR, M468, The University of Western Australia, 35 Stirling Highway, Crawley, Western Australia 6009, Australia

<sup>3</sup> Max-Planck Institut für extraterrestrische Physik, D-85741 Garching, Germany

<sup>4</sup> Max-Planck Institut für Astrophysik, D-85741 Garching, Germany

<sup>5</sup> University of the Western Cape, Bellville, Cape Town 7535, South Africa

<sup>6</sup> South African Astronomical Observatories, Observatory, Cape Town 7925, South Africa

<sup>7</sup> Institute for Astronomy, Royal Observatory, Edinburgh EH9 3HJ, UK

<sup>8</sup> Instituto Radioastronomía Milimétrica, Av. Divina Pastora 7, Nucleo Central, E-18012 Granada, Spain

<sup>9</sup> Johns Hopkins University, Baltimore, Maryland 21218, USA

<sup>10</sup> Centre for Astrophysics and Supercomputing, Swinburne University of Technology, Hawthorn, Victoria 3122, Australia

<sup>11</sup> Centre for Extragalactic Astronomy, Department of Physics, Durham University, South Road, Durham DH1 3LE, UK

<sup>12</sup> Department of Astronomy, Columbia University, New York, NY 10027, USA

<sup>13</sup> Institut de Radioastronomie Millimétrique, 300 Rue de la piscine, F-38406 St Martin d'Hères, France

<sup>14</sup> Kavli Institute for Astronomy and Astrophysics, Peking University, Beijing 100871, China

<sup>15</sup> Department of Physics, University of Bath, Claverton Down, Bath, BA2 7AY, UK

<sup>16</sup> School of Earth and Space Exploration, Arizona State University, Tempe, AZ 85287, USA

Received 2017 July 25; revised 2017 September 19; accepted 2017 October 2; published 2017 December 8

## Abstract

We introduce xCOLD GASS, a legacy survey providing a census of molecular gas in the local universe. Building on the original COLD GASS survey, we present here the full sample of 532 galaxies with CO (1–0) measurements from the IRAM 30 m telescope. The sample is mass-selected in the redshift interval  $0.01 < z < 0.05$  from the Sloan Digital Sky Survey (SDSS) and therefore representative of the local galaxy population with  $M_* > 10^9 M_\odot$ . The CO (1–0) flux measurements are complemented by observations of the CO (2–1) line with both the IRAM 30 m and APEX telescopes, HI observations from Arecibo, and photometry from SDSS, *WISE*, and *GALEX*. Combining the IRAM and APEX data, we find that the ratio of CO (2–1) to CO (1–0) luminosity for integrated measurements is  $r_{21} = 0.79 \pm 0.03$ , with no systematic variations across the sample. The CO (1–0) luminosity function is constructed and best fit with a Schechter function with parameters  $L_{\text{CO}}^* = (7.77 \pm 2.11) \times 10^9 \text{ K km s}^{-1} \text{ pc}^2$ ,  $\phi^* = (9.84 \pm 5.41) \times 10^{-4} \text{ Mpc}^{-3}$ , and  $\alpha = -1.19 \pm 0.05$ . With the sample now complete down to stellar masses of  $10^9 M_\odot$ , we are able to extend our study of gas scaling relations and confirm that both molecular gas fractions ( $f_{\text{H}_2}$ ) and depletion timescale ( $t_{\text{dep}}(\text{H}_2)$ ) vary with specific star formation rate (or offset from the star formation main sequence) much more strongly than they depend on stellar mass. Comparing the xCOLD GASS results with outputs from hydrodynamic and semianalytic models, we highlight the constraining power of cold gas scaling relations on models of galaxy formation.

**Key words:** galaxies: evolution – galaxies: ISM – galaxies: star formation – ISM: general

**Supporting material:** figure set, tar.gz file

## 1. Introduction

Much of galaxy evolution is regulated by the availability of gas and the efficiency of the star formation process out of this material. For example, the shape, tightness, and redshift evolution of the main sequence of star-forming galaxies in the star formation rate–stellar mass (SFR– $M_*$ ) plane can be explained by the availability of cold gas through inflows, the efficiency of the star formation process, and the balancing power of feedback (e.g., Bouché et al. 2010; Lilly et al. 2013; Tacconi et al. 2013, 2017; Sargent et al. 2014; Saintonge et al. 2016). The cold atomic and molecular gas in the interstellar medium (ISM) of galaxies is not only intimately linked to star formation but also an excellent probe of the larger environment and of evolutionary mechanisms.

While initially mostly restricted to particularly luminous or nearby galaxies (e.g., Sanders & Mirabel 1985; Radford

et al. 1991; Young et al. 1995; Solomon et al. 1997), over the past two decades samples of galaxies with integrated molecular line observations have grown to include in the local universe normal, noninteracting spiral galaxies (Braine et al. 1993; Sage 1993), cluster spiral galaxies (Kenney & Young 1988; Boselli et al. 1997), early-type galaxies (Combes et al. 2007; Krips et al. 2010; Young et al. 2011), galaxies with active nuclei (Helfer & Blitz 1993; Sakamoto et al. 1999; García-Burillo et al. 2003), and isolated galaxies (Lisenfeld et al. 2011). Improvements in instrument sensitivities and bandwidth have also made possible the investigation of the molecular gas contents of galaxies far beyond the local universe (Daddi et al. 2010; Tacconi et al. 2010; Geach et al. 2011; Magdis et al. 2012; Magnelli et al. 2012; Bauermeister et al. 2013).

The COLD GASS survey (CO Legacy Database for GASS; Saintonge et al. 2011a) was designed to provide a cohesive picture of molecular gas across the local galaxy population with

$M_* > 10^{10} M_\odot$ . Unlike all the studies mentioned above, the sample was selected purely by redshift and stellar mass rather than targeting specific classes of galaxies and, with 366 galaxies observed as part of a cohesive observing campaign, is homogeneous and large enough to statistically characterize scaling relations and their scatter. Significant results from COLD GASS include the demonstration that star formation efficiency varies systematically across the galaxy population (Saintonge et al. 2011b, 2012) and that the position of galaxies in the SFR– $M_*$  plane is driven by their gas contents and the varying star formation efficiency (Saintonge et al. 2016). Because the COLD GASS sample is large and unbiased, it serves as the perfect reference for studies of particular galaxy populations (e.g., active galactic nucleus [AGN] hosts, interacting galaxies, early-type galaxies) and has been extensively used as such (e.g., Fumagalli et al. 2012; Bothwell et al. 2014; Kirkpatrick et al. 2014; Shimizu et al. 2015; Stanway et al. 2015; Alatalo et al. 2016; Amorín et al. 2016; Yesuf et al. 2017). It is also an ideal  $z = 0$  reference point for studies of molecular gas at higher redshifts (e.g., Combes et al. 2013; Troncoso et al. 2014; Genzel et al. 2015; Seko et al. 2016; Tacconi et al. 2017) and provides powerful constraints for theoretical models and numerical simulations (e.g., Lagos et al. 2011; Genel et al. 2014; Lagos et al. 2015; Popping et al. 2015; Davé et al. 2017).

Until now, COLD GASS could only provide information for the relatively massive galaxy population ( $M_* > 10^{10} M_\odot$ ). Recognizing the need to understand the link between gas, star formation, and global galaxy properties in lower-mass galaxies, we launched a second IRAM 30 m large program to extend the sample down to stellar masses of  $10^9 M_\odot$ . We present here the combination of the two surveys, now collectively referred to as xCOLD GASS for “extended COLD GASS”; it contains IRAM 30 m CO (1–0) measurements and a wide range of measured global properties for 532 galaxies spanning the entire SFR– $M_*$  plane at  $M_* > 10^9 M_\odot$ .

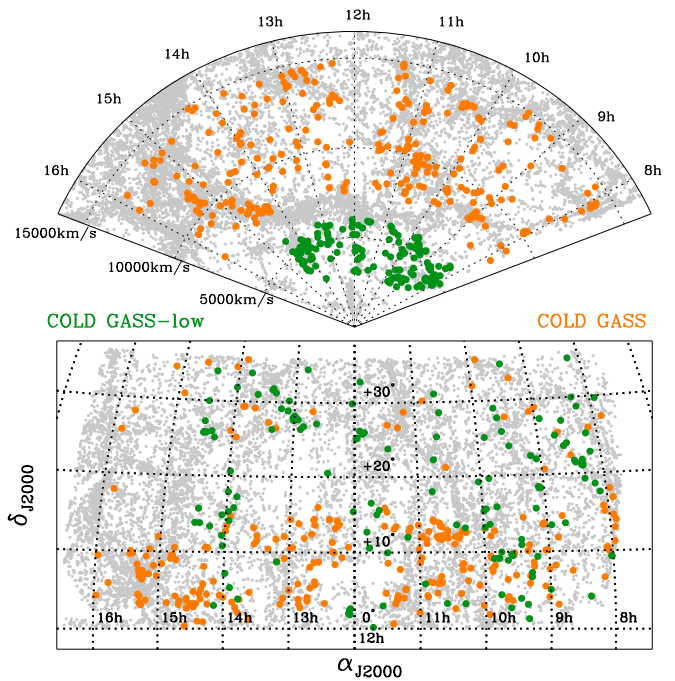
This paper presents the full catalog of IRAM 30 m measurements, including both CO (1–0) and CO (2–1) line fluxes, complementary APEX CO (2–1) observations, and a catalog of global galaxy measurements derived from *GALEX*, Sloan Digital Sky Survey (SDSS), and *WISE* data products. We then use the xCOLD GASS sample to derive a robust CO luminosity function; determine the CO (2–1)/CO (1–0) excitation correction; present the extended scaling relations between gas fraction, depletion timescales, and global galaxy properties; and conclude by discussing the key role of molecular gas observations in understanding the multiscale nature of the star formation process and in providing fresh and important constraints for models of galaxy formation.

All rest-frame and derived quantities in this work assume a Chabrier (2003) initial mass function and a cosmology with  $H_0 = 70 \text{ km s}^{-1} \text{ Mpc}^{-1}$ ,  $\Omega_m = 0.3$ , and  $\Omega_\Lambda = 0.7$ .

## 2. Sample and Observations

### 2.1. Two IRAM Large Programs

The xCOLD GASS sample was assembled over the course of two large programs at the IRAM 30 m telescope. The initial COLD GASS survey targeted 366 galaxies with  $M_* > 10^{10} M_\odot$  and  $0.025 < z < 0.050$ . The sample was selected randomly out of the complete parent sample of SDSS galaxies within the ALFALFA footprint matching these



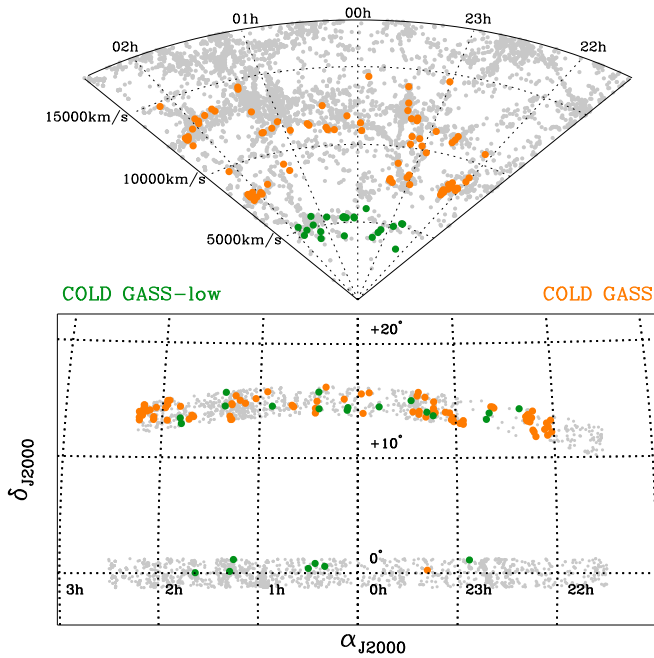
**Figure 1.** Distribution of the “Spring” component of the sample ( $8 \text{ hr} < \alpha_{J2000} < 16.0 \text{ hr}$ ) in the redshift–right ascension plane (top) and as projected on the sky (bottom).

criteria, making it unbiased and representative of the local galaxy population. A thorough description of the sample selection, survey strategy, and scientific motivation is given in Saintonge et al. (2011a).

The original COLD GASS survey was followed by a second effort, to extend the sample in the stellar mass range of  $10^9 < M_*/M_\odot < 10^{10}$ ; we refer to this second survey as COLD GASS-low. Since the predicted CO luminosities of these galaxies are lower, the redshift range was lowered to  $0.01 < z < 0.02$  for ease of detection. In this redshift range, the SDSS spectroscopic sample is complete for galaxies with  $M_* > 10^9 M_\odot$ , and the angular sizes of these lower-mass galaxies are small enough that most of the CO flux can be recovered with a single pointing of the IRAM 30 m telescope and a small aperture correction. A random subsample of 166 galaxies from the SDSS parent sample of 764 galaxies was targeted with IRAM.

The combined xCOLD GASS sample therefore contains 532 galaxies with IRAM 30 m CO (1–0) observations. The distributions of these objects on the sky and in redshift space are shown in Figures 1 and 2. The redshift range of each survey is such that all sources could be observed with a single frequency tuning. Furthermore, the large footprint of the survey meant that observations could be performed at almost any time (and under almost any weather conditions), making the programs ideal for pool observing, while the high density of sources on the sky implied that nearby sources could be observed without the need for major repointing/focusing of the telescope. These three elements were critical in enabling a very high observing efficiency and the assembly of a large sample (532 galaxies over a total of  $\sim 950$  hr of observing time).

Both the sample selection and the observing strategy make xCOLD GASS the ideal sample to build scaling relations and serve as the benchmark for galaxy evolution studies. Such key



**Figure 2.** Distribution of the “Fall” component of the sample ( $22 \text{ hr} < \alpha_{J2000} < 2.5 \text{ hr}$ ) in the redshift–right ascension plane (top) and as projected on the sky (bottom).

features are (1) the representative nature of the sample, being purely mass selected with no additional cuts on quantities such as SFR, morphology, or infrared luminosity; (2) the size of the sample, which allows us to define both mean scaling relations and any scatter or third-parameter dependencies; (3) the homogeneity of the CO measurements and the strict upper limits set in the case of nondetections; and (4) the large dynamic range of the various physical properties under consideration (e.g., 2.5 dex in stellar mass, and metallicities ranging from 0.2 to  $1.1Z_{\odot}$ ).

## 2.2. Galaxy Properties and Ancillary Observations

For each survey, the sample was randomly selected out of the SDSS parent sample to have a flat  $\log M_{\odot}$  distribution to ensure an even sampling of the stellar mass parameter space. However, since the underlying stellar mass distribution of the full sample from SDSS is very well characterized, we can easily correct for this “mass bias” (Catinella et al. 2010). As a starting point, we construct the expected mass distribution of a purely volume-limited sample of 532 galaxies based on the Baldry et al. (2012) stellar mass function; this is the orange dashed line in Figure 3(a), to be compared with the actual mass distribution of the xCOLD GASS sample, shown as the filled gray histogram. We assign as a statistical weight to each galaxy within  $\log M_{*}$  bins of 0.1 dex in width the ratio between the number of galaxies expected from the stellar mass function and the number of objects in the xCOLD GASS sample (i.e., the weight as a function of  $\log M_{*}$  is the ratio between the orange dashed histogram and the filled gray histogram of Figure 3(a)). To illustrate the impact of this weighting on other key parameters, Figure 3 shows the difference between the observed distribution of stellar mass surface density, near-UV (NUV)– $r$  color, and metallicity for the xCOLD GASS sample before and after the weights are taken into consideration (filled

gray and black solid line histograms, respectively). Any scaling relation or mean quantity presented in this paper takes these weights into account, as they make the xCOLD GASS sample volume-limited.

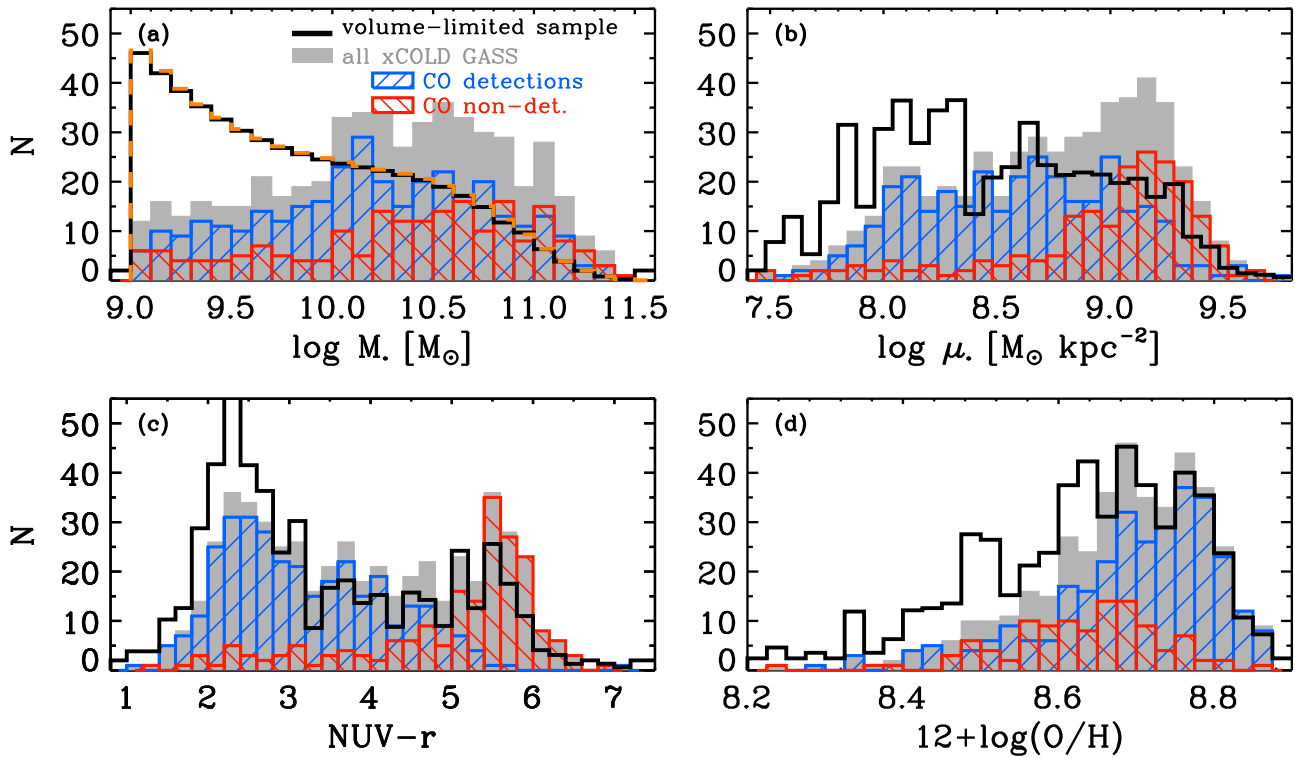
To derive accurate SFRs for all xCOLD GASS galaxies, photometry is extracted from the *WISE* and *GALEX* survey databases. The IR and UV components of the total SFR are calculated and combined following exactly the method described in Janowiecki et al. (2017). We also extract information from the SDSS DR7 database to provide us with information about the structural properties and chemical composition of the galaxies. For all the xCOLD GASS objects, the following key parameters are given in Table 1:

1. **GASS ID**: catalog ID in the GASS survey. Galaxies with six digit IDs are part of COLD GASS-low.
2.  $\alpha_{J2000}$ : R.A. of the SDSS object, in decimal degrees.
3.  $\delta_{J2000}$ : decl. of the SDSS object, in decimal degrees.
4. **Redshift**: SDSS spectroscopic redshift.
5. **Stellar mass**: stellar mass from the SDSS DR7 MPA/JHU catalog.<sup>17</sup>
6. **Stellar mass surface density**: calculated as  $\mu_{*} = M_{*}(2\pi r_{50,z}^2)^{-1}$ , where  $r_{50,z}$  is the radius encompassing 50% of the  $z$ -band flux, in kpc. Galaxies with  $\log \mu_{*} > 8.7$  are considered to have a significant stellar bulge.
7. **Concentration index**: ratio of the  $r$ -band Petrosian radii encompassing 90% and 50% of the flux,  $C = r_{90,r}/r_{50,r}$ . The concentration index can be regarded as a proxy for the bulge-to-disk ratio (Weinmann et al. 2009), with  $C > 2.5$  being bulge-dominated galaxies.
8. **Effective radius**: SDSS  $r$ -band major axis effective radius, in kpc.
9. **NUV– $r$  color**: calculated from resolution-matched SDSS and *GALEX* photometry (see Wang et al. 2010) and corrected for Galactic extinction using the prescription of Wyder et al. (2007).
10. **SFR**: calculated using an “SFR ladder” technique as described in Janowiecki et al. (2017).
11. **Metallicity**: gas-phase metallicity  $12 + \log \text{O}/\text{H}$  using both the  $[\text{N II}]/\text{H}\alpha$  and  $[\text{O III}]/\text{H}\beta$  line ratios and the calibration of Pettini & Pagel (2004), for the galaxies classified as star-forming or composite in the BPT diagram (see next column). For galaxies with either weak emission lines or AGN activity, the metallicity is inferred from the mass–metallicity relation derived by Kewley & Ellison (2008) to be consistent with the strong line calibration of Pettini & Pagel (2004).
12. **BPT classification**: spectral classification based on the BPT diagram. 0: inactive; 1: star-forming; 2: composite; 3: AGN/LINER; 4: Seyfert; –1: undetermined.

## 2.3. xGASS: The Atomic Gas Survey

Just like in the case of the original COLD GASS, the new COLD GASS-low survey was accompanied by a sister program at the Arecibo telescope (PI: B. Catinella). When available, HI masses are taken from the ALFALFA blind survey catalog (Giovanelli et al. 2005; Haynes et al. 2011), or else they are observed with Arecibo as part of this program.

<sup>17</sup> <http://home.strw.leidenuniv.nl/~jarle/SDSS/>



**Figure 3.** Distributions of some key parameters across the xCOLD GASS sample: (a) stellar mass, (b) stellar mass surface density, (c) NUV- $r$  color, and (d) gas-phase metallicity calculated using the O3N2 calibration of Pettini & Pagel (2004). In all panels, the filled gray histogram shows the distribution for the 532 xCOLD GASS objects. Galaxies with CO (1-0) detection and nondetection are shown separately as the blue and red histograms, respectively. The solid black line shows the distribution of the xCOLD GASS sample after weights are applied to correct for the flat  $\log M_*$  distribution in the observed samples; this matches the stellar mass function as shown by the orange dashed line in panel (a). Using the weighting, the xCOLD GASS sample can therefore be considered to be volume-limited.

The GASS survey measured the HI content for  $\sim 700$  galaxies with stellar masses greater than  $10^{10} M_\odot$  and redshifts between 0.025 and 0.050 using the Arecibo radio telescope (Catinella et al. 2010, 2012a, 2012b). Galaxies were selected from SDSS DR6, with the additional requirement on the sky footprint to be covered by projected GALEX MIS and ALFALFA surveys. Observations were limited to a gas fraction  $M_{\text{HI}}/M_*$  between 2% and 5%, depending on stellar mass.

The low-mass extension, GASS-low, targeted  $\sim 200$  galaxies with the same stellar mass and redshift cuts as COLD GASS-low, selected from SDSS DR7 and lying within the ALFALFA 70% footprint (Catinella et al. 2017). Observations were limited to gas fractions between 2% and 10%.

In order to increase survey efficiency, galaxies with good detections from the ALFALFA survey were not reobserved; hence, the observed sample lacked HI-rich objects. This was corrected by adding the correct proportion of randomly selected ALFALFA galaxies, based on the ALFALFA detection fraction in each stellar mass bin. This procedure applied to both GASS and GASS-low volumes yields the xGASS *representative sample*, hereafter simply referred to as xGASS, which includes 1179 galaxies—of these, 68% are HI detections. The GASS representative sample was revisited to take advantage of more accurate ALFALFA detection fractions, now available for larger volumes, and to maximize overlap with xCOLD GASS (see Catinella et al. 2017, for details). The overlap between xGASS and xCOLD GASS includes 477 galaxies; the HI detection fraction for this subset is 73%.

#### 2.4. IRAM 30 m Observations and Data Reduction

All xCOLD GASS observations of the CO (1-0) line were carried out at the IRAM 30 m telescope using the Eight Mixer Receiver (EMIR; Carter et al. 2012). In the 3 mm band (E090), we can make use of two sidebands each with a bandwidth of 8 GHz per linear polarization. For each survey, the E090 band was tuned to a specific frequency that allowed us to detect the redshifted CO (1-0) line for all galaxies within the available bandwidth. The second band was tuned to a fixed frequency in the 1 mm (E230) band to cover the redshifted CO (2-1) line that fell within the available 4 GHz bandwidth for 68% of our sample. All details regarding the setup of the instruments during both surveys are presented in Table 2.

All observations were done in wobbler-switching mode. For the initial survey, we used the Wideband Line Multiple Autocorrelator (WILMA) as the primary back end, with the 4 MHz Filterbank as a backup. This allowed for simultaneous coverage of 4 GHz of bandwidth in each linear polarization and for each band. For COLD GASS-low we were able to take advantage of the new Fourier Transform Spectrometer (FTS), making it possible to record the full 8 GHz of bandwidth from EMIR. The spectral resolution of the FTS is also a factor of 10 higher. The beam size of the telescope is  $22''$  at 3 mm and  $11''$  at 1 mm.

The observing for xCOLD GASS took place between 2009 and 2015, with widely different atmospheric conditions. The strategy was to observe the galaxies predicted to be the most CO luminous under poorer weather conditions, as these require a typical rms sensitivity of 1.5–2.0 mK per  $20 \text{ km s}^{-1}$  channel

**Table 1**  
Identifiers and Properties of the xCOLD GASS Galaxies

ID	$\alpha_{J2000}$ (deg)	$\delta_{J2000}$ (deg)	$z_{\text{spec}}$	$\log M_*$ ( $\log M_\odot$ )	$\log \mu_*$ ( $\log M_\odot \text{ kpc}^{-2}$ )	$C$	$r_{50}$ (kpc)	NUV- $r$	SFR ( $M_\odot \text{ yr}^{-1}$ )	12 +log O/H	BPT Class
124028	1.50998	14.41746	0.0176	9.11	7.71	2.39	2.47	2.96	0.14	8.48	1
124012	1.62208	14.18237	0.0178	9.74	8.27	2.42	2.42	4.37	0.16	8.62	0
11956	2.08654	15.15601	0.0395	10.09	8.55	2.15	2.42	3.04	0.47	8.72	1
12025	4.89396	16.20418	0.0366	10.84	9.19	3.03	2.85	5.93	0.21	8.77	3
124006	4.94721	0.59079	0.0177	9.75	8.76	3.15	1.21	3.57	0.55	8.62	4
124000	5.93277	14.30672	0.0179	9.41	7.96	2.22	2.60	2.62	0.22	8.58	1
124010	5.99747	15.77045	0.0177	9.93	8.18	2.14	4.12	2.04	2.94	8.80	1
12002	6.26670	14.97091	0.0367	10.48	9.47	3.17	1.32	6.25	0.01	8.76	-1
124004	6.39337	0.84685	0.0178	9.31	1.39	1.00	...	2.18	0.33	8.72	1
11989	6.49538	13.92940	0.0419	10.69	9.25	3.02	2.20	5.79	0.04	8.77	3
11994	6.49573	14.34799	0.0373	10.17	8.12	2.43	4.82	2.53	0.91	8.70	1
124003	7.40992	0.41037	0.0138	9.22	7.76	1.95	2.43	1.82	0.30	8.48	1
27167	9.84028	14.46986	0.0380	10.37	9.21	2.77	1.62	4.48	0.16	8.75	3
3189	10.09787	14.61375	0.0384	10.05	7.99	1.96	4.54	2.77	2.37	8.69	0
124027	13.11632	14.51829	0.0182	9.78	8.03	2.11	4.09	2.91	0.53	8.70	1
3261	13.88588	15.77582	0.0375	10.08	8.63	2.54	2.25	2.63	1.49	8.73	1
3318	15.65954	15.16852	0.0397	10.53	9.04	3.05	2.29	5.73	0.07	8.76	0
3439	17.27486	14.75578	0.0386	10.35	8.84	2.90	2.72	3.05	0.52	8.74	3
3465	18.09092	15.01085	0.0292	10.19	8.98	2.89	1.80	3.63	0.22	8.72	3
101025	18.65576	1.18149	0.0154	9.84	8.02	1.71	3.96	2.84	0.45	8.76	1
3645	18.75730	15.41350	0.0307	10.33	8.98	2.71	1.98	3.97	0.15	8.74	3
101021	19.22327	0.15313	0.0190	9.22	8.00	2.19	1.93	2.33	0.28	8.67	1
3509	19.29855	13.34094	0.0484	10.81	9.26	3.11	2.54	4.14	1.24	8.75	2
3524	19.31707	14.62238	0.0380	10.73	9.42	2.71	2.01	5.15	0.32	8.68	2
3519	19.36713	14.70443	0.0427	10.74	8.71	2.20	4.48	3.68	3.01	8.79	1
3505	19.44485	13.32348	0.0479	10.21	8.91	3.30	1.87	4.92	0.25	8.72	-1
3504	19.59767	13.62457	0.0380	10.16	7.98	1.84	6.43	2.85	0.74	8.71	0
101007	20.28890	15.69477	0.0171	9.45	7.88	1.75	3.01	2.26	0.54	8.64	1
101004	20.37777	14.50498	0.0140	9.92	8.78	2.30	1.67	2.84	0.63	8.79	1
101037	24.40472	0.04017	0.0164	9.31	8.00	2.48	2.14	2.14	0.32	8.60	1

**Note.** The full version of this table, including all columns and all 532 xCOLD GASS galaxies from Tables 1, 3, and 4 is available online in a machine-readable FITS format. A detailed description of this table's contents is given in Section 2.2.

**Table 2**  
xCOLD GASS IRAM 30 m Observing Parameters

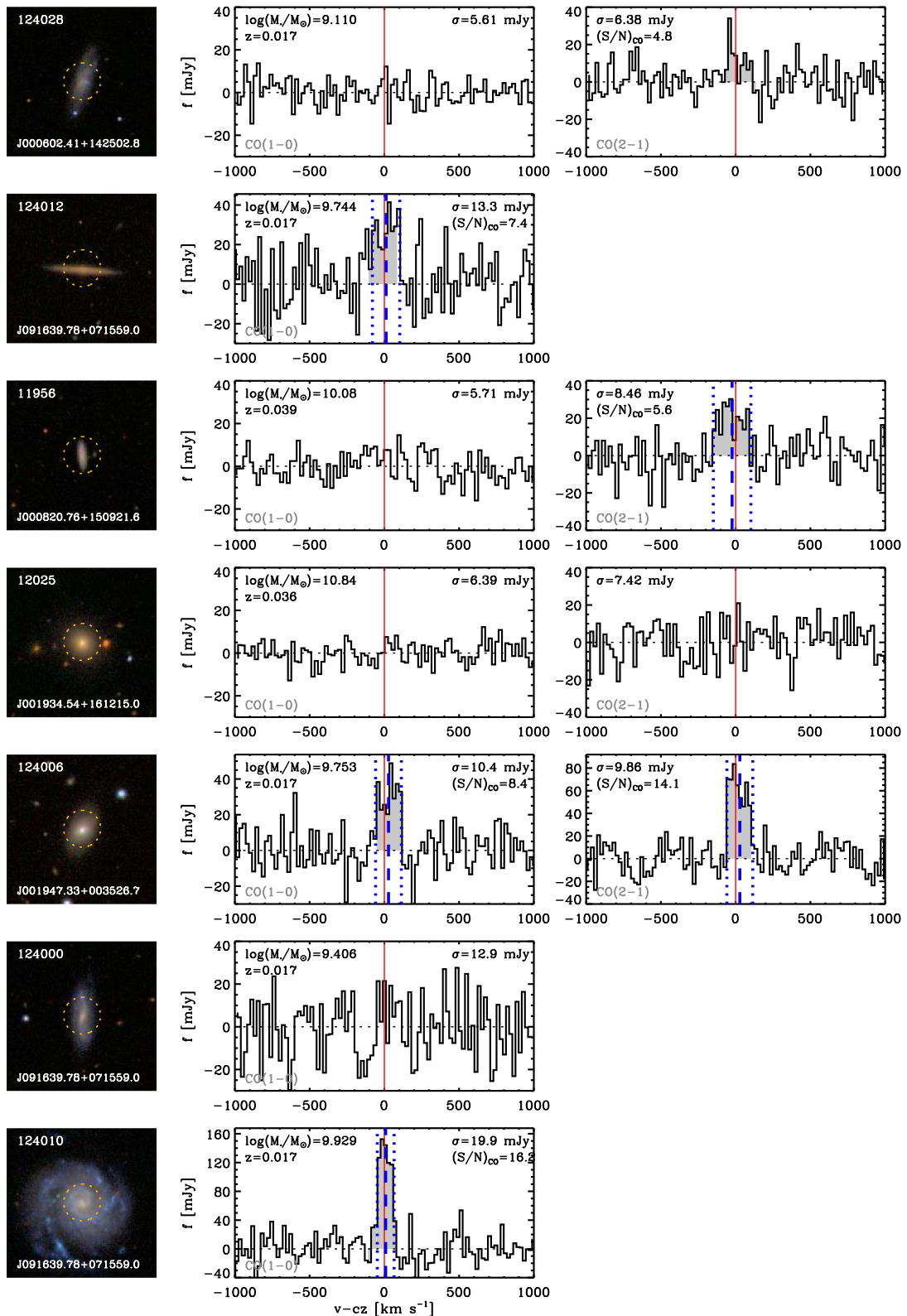
	COLD GASS	COLD GASS-low
Observing period	2009 Jun–2011 Dec	2012 Jul–2017 May
Front end	EMIR	EMIR
Back end	WILMA and 4 MHz Filterbank	FTS
E090 frequency	109.3–113.0 GHz	107.4–115.2 GHz
E230 frequency	220.7–224.4 GHz	224.7–232.5 GHz
Spectral resolution	2 MHz	0.1953 MHz
Wobbler frequency/ throw	1 Hz/180''	1 Hz/120''

to achieve a detection of CO (1–0) with signal-to-noise ratio ( $S/N$ )  $> 5$ . When the precipitable water level was particularly low, we favored the redder galaxies (predicted to be CO faint) in order to achieve rms sensitivities of 0.8–1.0 mK in a reasonable amount of time (average of  $\sim 2$  hr per target). The overall strategy was to observe a galaxy until either the CO (1–0) line was detected with  $S/N > 5$  or the rms noise was low enough to allow us to put a stringent upper limit on the gas fraction of  $M_{\text{H}_2}/M_* = 1.5\%$  for COLD GASS and 2.5% for COLD GASS-low.

The IRAM data were all reduced with the CLASS software. Individual scans were baseline-subtracted (first-order fit, excluding the spectral region within  $\pm 300 \text{ km s}^{-1}$  of the

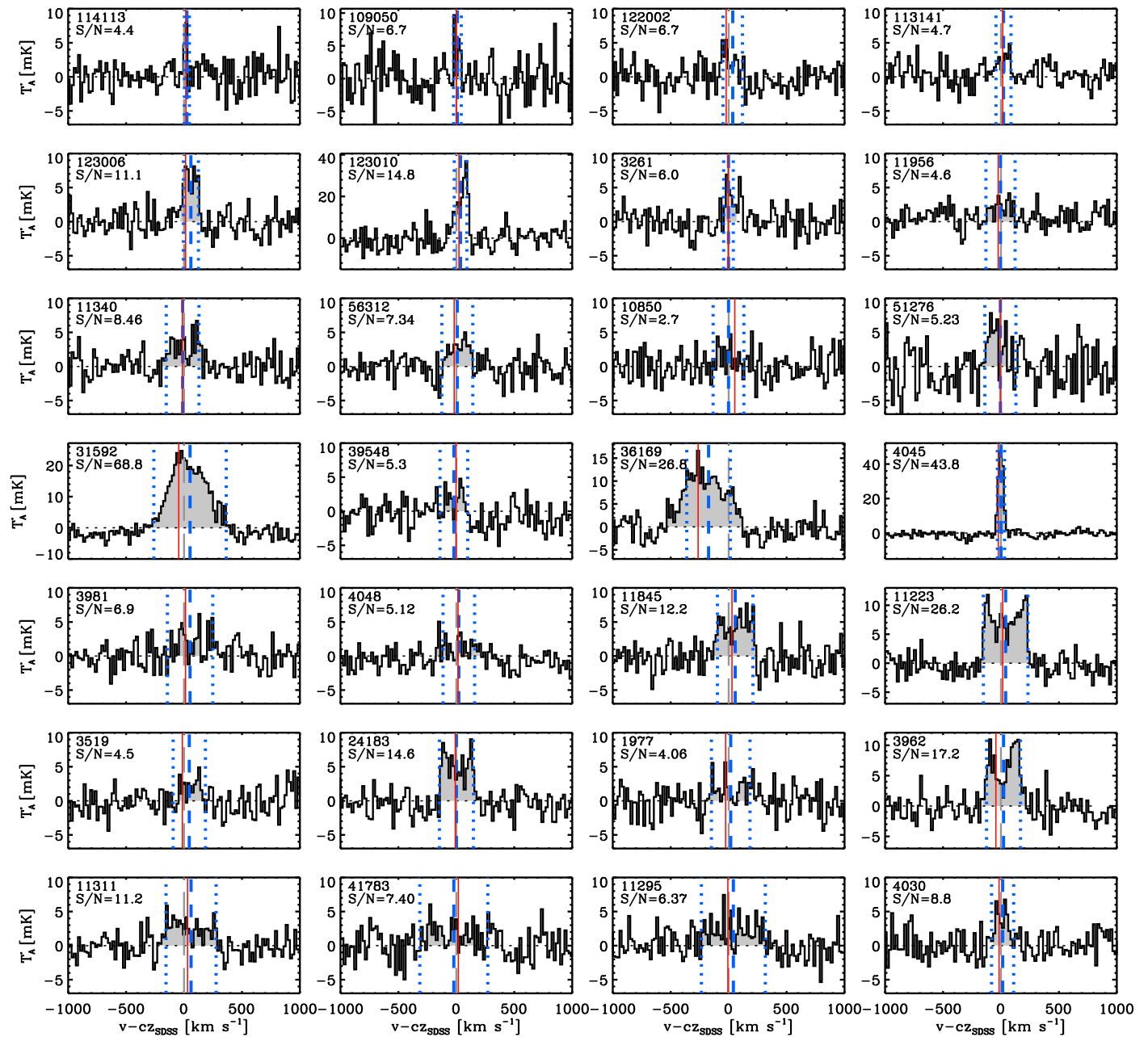
expected line center based on the optical redshift), visually examined to reject those with distorted baselines or anomalous features, and combined into a final averaged spectrum binned to a resolution of  $20 \text{ km s}^{-1}$ . Example IRAM 30 m spectra are shown in Figure 4, alongside the optical SDSS image of each galaxy. A spectral window is defined for each emission line to match the observed line width. In cases where the CO line is undetected, the window is set either to the width of the H I line or to a width of  $300 \text{ km s}^{-1}$  ( $200 \text{ km s}^{-1}$  for COLD GASS-low) if no H I information is available. The integrated line flux,  $S_{\text{CO,obs}}$ , is measured by adding the signal within this spectral window, and the standard deviation of the noise per  $20 \text{ km s}^{-1}$  channel,  $\sigma_{\text{rms}}$ , is measured outside of it. Properties of the spectral lines, such as central velocity and width, are measured using a custom-made IDL interactive program following the technique described in, e.g., Springob et al. (2007), Catinella et al. (2007), and Saintonge et al. (2011a). For the galaxies with the highest  $S/N$ , a second width-fitting scheme is applied, allowing for careful error estimation as is required for Tully–Fisher work (Tiley et al. 2016).

Given the angular size of the galaxies, most of their flux can be recovered by a single pointing of the IRAM 30 m telescope. However, to account for the larger angular size of some of the galaxies, we apply an aperture correction to all of the measured CO (1–0) line fluxes. The method presented in Saintonge et al. (2012) is used. In short, for each xCOLD GASS object, a



**Figure 4.** SDSS images and IRAM 30 m spectra of the xCOLD GASS galaxies. Each SDSS image is  $1/5 \times 1/5$  in dimension and shows the position and size of the IRAM 30 m beam at the frequency of the CO (1–0) line (the diameter of the beam is half of that at the frequency of the CO (2–1) line). The middle panel shows the IRAM spectrum detected centered on the position of the CO (1–0) line. The solid red line is the expected center of the line based on the SDSS spectroscopic redshift. When the CO line is detected, the dashed blue line indicates the central velocity of the line and the dotted lines represent the FWHM of the line based on the fitting technique described in Section 2.5. The gray shaded area represents the region of the spectrum over which we integrated to calculate the total line flux. The right panel shows the IRAM spectrum centered on the CO (2–1) line when those observations are available. The complete figure set (76 images) is available in the online journal.

(The complete figure set (76 images) is available.)



**Figure 5.** APEX CO (2–1) spectra of xCOLD GASS objects. Shown are the 28 galaxies from Table 4 with detections of the CO (2–1) line. In each panel, the red solid line is the expected line center based on the SDSS optical redshift, while the dashed and dotted blue vertical lines are the measured CO line center and width, respectively. The gray shaded areas represent the region of the spectra over which we integrated to calculate the total line flux.

model galaxy is created assuming an exponential molecular gas disk with a scale length equivalent to the radius enclosing half of the SFR. The model is given the inclination of the real galaxy and then convolved with a Gaussian matching the properties of the IRAM beam. The aperture correction is the ratio between the flux of the model before and after this convolution. The median aperture correction across the xCOLD GASS sample is 1.17. We performed tests to ensure that the scaling relations presented later in this paper are not caused by inadequate aperture corrections by confirming that key quantities that should not depend on distance within our sample (such as molecular gas fraction and depletion timescale) are indeed uncorrelated.

### 2.5. IRAM Catalog Description

Based on the line fluxes, widths, and spectral noise measurements described above, we introduce the full catalog of CO (1–0) and CO (2–1) measurements for all 532 xCOLD GASS. As presented in Table 3, the catalog includes the following quantities:

1. **GASS ID**: catalog ID in the GASS survey. Galaxies with six-digit IDs are part of COLD GASS-low.
2.  $\sigma_{\text{CO}10}$ : rms noise achieved around the CO (1–0) line, in spectral channels with width  $\Delta w_{\text{ch}} = 20 \text{ km s}^{-1}$ .
3. **FlagCO10**: detection flag for the CO (1–0) line. 1: detection; 2: nondetection. In the cases where the line is

not detected, the line luminosities and molecular gas mass given in columns (7), (8), and (20) are  $3\sigma$  upper limits.

4.  $S/N_{\text{CO}10}$ : signal-to-noise ratio achieved in the CO (1–0) line, calculated as  $S_{\text{CO}10,\text{obs}}/\epsilon_{\text{obs}}$ , where

$$\epsilon_{\text{obs}} = \frac{\sigma_{\text{CO}10} W50_{\text{CO}10}}{\sqrt{W50_{\text{CO}10} \Delta w_{\text{ch}}^{-1}}}, \quad (1)$$

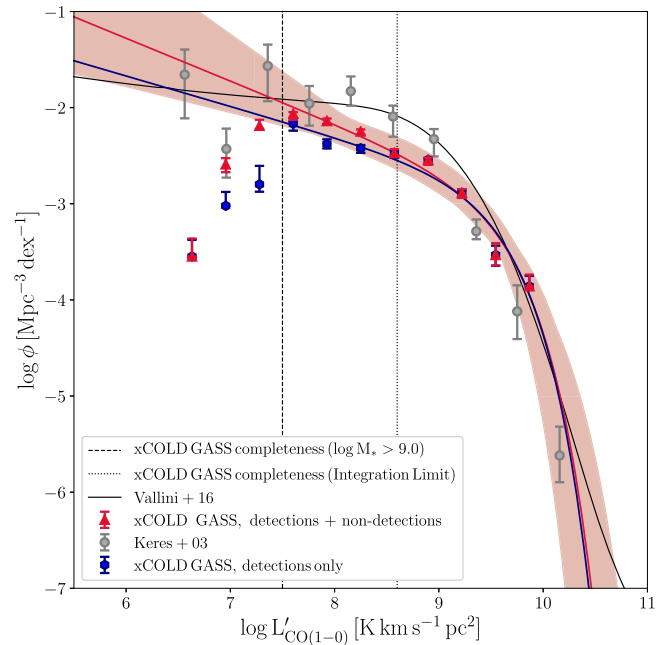
where  $\Delta w_{\text{ch}} = 20 \text{ km s}^{-1}$  is the spectral channel width,  $\sigma_{\text{CO}10}$  is the rms noise (see Column (2)), and  $W50_{\text{CO}10}$  is the line width (see Column (10)).

5.  $S_{\text{CO}10,\text{obs}}$ : integrated CO (1–0) line flux within the IRAM beam, measured as described in Section 2.4. The values are given in units of  $\text{Jy km s}^{-1}$ , after applying the point-source sensitivity factors recommended for EMIR.<sup>18</sup>
6.  $S_{\text{CO}10,\text{cor}}$ : total CO (1–0) line flux, calculated from  $S_{\text{CO}10,\text{obs}}$  and the galaxy-specific aperture correction, as described in Section 2.4. This is the flux value recommended to be used to infer the total molecular gas mass of the xCOLD GASS galaxies.
7.  $L'_{\text{CO}10,\text{obs}}$ : beam-integrated CO (1–0) line luminosity in units of  $\text{K km s}^{-1} \text{ pc}^2$  calculated following Solomon et al. (1997):

$$L'_{\text{CO}10,\text{obs}} = 3.25 \times 10^7 S_{\text{CO}10,\text{obs}} \nu_{\text{obs}}^{-2} D_L^2 (1+z)^{-3}, \quad (2)$$

where  $\nu_{\text{obs}}$  is the observed frequency of the CO (1–0) line in GHz and  $D_L$  is the luminosity distance in units of Mpc. The error includes the measurement uncertainty and the 8% flux calibration error at these frequencies. Uncertainties on pointing and redshift are negligible in comparison and not included (Saintonge et al. 2011a). If  $\text{FlagCO}10 = 2$  (see Column (3)), then the value is a  $3\sigma$  upper limit, where  $\sigma$  is calculated using Equation (1) assuming that  $W50_{\text{CO}10} = W50_{\text{H}1}$  when an H I detection is available, otherwise constant values of 300 and 200  $\text{km s}^{-1}$  for galaxies with  $M_*$  greater and lower than  $10^{10} M_{\odot}$ , respectively.

8.  $L'_{\text{CO}10,\text{cor}}$ : total CO (1–0) line luminosity, calculated from  $L'_{\text{CO}10,\text{obs}}$  and the aperture correction. The error includes the measurement uncertainty, the 8% flux calibration error, and the 15% uncertainty on the aperture correction (Saintonge et al. 2012). If  $\text{FlagCO}10 = 2$  (see Column (3)), then the value is a  $3\sigma$  upper limit.
9.  $z_{\text{CO}10}$ : redshift of the galaxy based on the central velocity of the CO (1–0) line.
10.  $W50_{\text{CO}10}$ : FWHM of the CO (1–0) line in  $\text{km s}^{-1}$ , calculated using the technique of Springob et al. (2005), which is based on fitting linear slopes to the two sides of the emission line and finding the width at half maximum along these fits.
11.  $W50_{\text{TER}}$ : FWHM of the CO (1–0) line in  $\text{km s}^{-1}$ , calculated for the galaxies with the highest S/N for the purpose of Tully–Fisher studies by fitting the emission lines with a Gaussian double-peak function (Tiley et al. 2016).
12.  $\sigma_{\text{CO}21}$ : rms noise achieved around the CO (2–1) line, in spectral channels with width  $\Delta w_{\text{ch}} = 20 \text{ km s}^{-1}$ . Since the integration times were set by the requirements to detect the CO (1–0) line, the depth of these observations



**Figure 6.** CO (1–0) luminosity from the xCOLD GASS sample, where  $\log L'_{\text{CO}}$  is given in units of  $\text{K km s}^{-1} \text{ pc}^2$ . The LF is shown if detections and the upper limits from nondetections are included (red triangles) and if only detections are used (blue hexagons). The best-fit Schechter function for the total xCOLD GASS sample where the data is complete is shown as a red line. For comparison the observed CO LF of local galaxies from Keres et al. (2003) (gray circles) and the empirical prediction for the CO LF using the  $\log L'_{\text{CO}} - L_{\text{IR}}$  conversion from Vallini et al. (2016) (solid black line) are also presented. The xCOLD GASS sample is complete down to  $\log L'_{\text{CO}} = 7.5$ .

is variable, as these frequencies are far more susceptible to elevated levels of atmospheric water vapor.

13.  $\text{FlagCO}21$ : detection flag for the CO (2–1) line. 0: not targeted; 1: detection; 2: nondetection. In the cases where the line is not detected, the CO (2–1) line luminosity in Column (16) is a  $3\sigma$  upper limit.
14.  $S/N_{\text{CO}21}$ : signal-to-noise ratio achieved in the CO (2–1) line, calculated as described for Column (3).
15.  $S_{\text{CO}21,\text{obs}}$ : integrated CO (2–1) line flux within the IRAM beam, in  $\text{Jy km s}^{-1}$ . Note that the beam size at these frequencies is half the size of that at the frequency of the CO (1–0) line. For this reason, the aperture correction to extrapolate the CO (2–1) to a total value is large and more uncertain; therefore, we only provide observed beam quantities for this line.
16.  $L'_{\text{CO}21,\text{obs}}$ : beam-integrated CO (2–1) line luminosity, in  $\text{K km s}^{-1} \text{ pc}^2$  calculated as described in Column (7).
17.  $z_{\text{CO}21}$ : redshift of the galaxy based on the central velocity of the CO (2–1) line.
18.  $W50_{\text{CO}21}$ : FWHM of the CO (2–1) line in  $\text{km s}^{-1}$ , calculated as in Column (10).
19.  $\alpha_{\text{CO}}$ : recommended value for the CO-to- $\text{H}_2$  conversion factor, calculated using the function calibrated by Accurso et al. (2017). This is a metallicity-dependent conversion function, with a second-order dependence on the offset of a galaxy from the star-forming main sequence.
20.  $\log M_{\text{H}_2}$ : total molecular gas mass, including the helium contribution, calculated from the total CO (1–0) line luminosity presented in Column (8) and the conversion function in Column (19) as

<sup>18</sup> <http://www.iram.es/IRAMES/mainWiki/EmirforAstronomers>



**Table 3**  
IRAM CO (1–0) and CO (2–1) Measurements

ID	$\sigma_{\text{CO10}}$ (mK)	FlagCO10	S/N <sub>CO10</sub>	$L'_{\text{CO10,cor}}$ ( $10^8 \text{ K km/s pc}^2$ )	$z_{\text{CO10}}$	$W50_{\text{CO10}}$ ( $\text{km s}^{-1}$ )	$\sigma_{\text{CO21}}$ (mK)	FlagCO21	S/N <sub>CO21</sub>	$L'_{\text{CO21,obs}}$ ( $10^8 \text{ K km/s pc}^2$ )	$z_{\text{CO21}}$	$\alpha_{\text{CO}}^a$	$\log M_{\text{H}_2}$ ( $\log M_{\odot}$ )
124028	0.94	2	...	0.22	...	...	1.06	1	4.85	$0.08 \pm 0.02$	0.01769	9.17	8.30
124012	2.22	1	7.46	$1.12 \pm 0.24$	0.01780	182.9	...	...	...	...	...	5.21	$8.77 \pm 0.18$
11956	0.95	2	...	1.05	...	...	1.41	1	5.68	$0.81 \pm 0.22$	0.03951	3.67	8.59
12025	1.06	2	...	1.12	...	...	1.24	2	...	0.35	...	2.86	8.51
124006	1.74	1	8.44	$0.85 \pm 0.18$	0.01779	173.2	1.64	1	14.13	$0.37 \pm 0.08$	0.01777	5.56	$8.68 \pm 0.18$
124000	2.16	2	...	0.50	...	...	...	...	...	...	...	6.31	8.50
124010	3.32	1	16.23	$4.51 \pm 0.81$	0.01774	112.7	...	...	...	...	...	3.15	$9.15 \pm 0.17$
12002	1.18	2	...	1.11	...	...	1.46	2	...	0.42	...	3.20	8.55
124004	1.95	1	5.11	$0.42 \pm 0.11$	0.01782	65.6	2.43	2	...	0.05	...	3.84	$8.21 \pm 0.19$
11989	1.07	2	...	1.20	...	...	2.14	2	...	0.80	...	2.86	8.54
11994	1.55	1	4.77	$2.73 \pm 0.74$	0.03721	276.9	3.08	2	...	0.87	...	4.00	$9.04 \pm 0.19$
124003	0.87	2	...	0.09	...	...	1.07	1	6.61	$0.05 \pm 0.01$	0.01380	9.44	7.91
27167	1.17	2	...	1.05	...	...	2.04	2	...	0.57	...	3.15	8.52
3189	1.24	1	5.99	$2.69 \pm 0.64$	0.03833	238.6	2.40	1	3.22	$0.67 \pm 0.25$	0.03840	4.53	$9.09 \pm 0.18$
124027	2.13	1	4.43	$0.93 \pm 0.26$	0.01820	220.0	4.03	1	5.15	$0.27 \pm 0.08$	0.01829	4.10	$8.58 \pm 0.20$
3261	1.96	1	8.57	$3.06 \pm 0.63$	0.03746	83.3	2.36	1	11.60	$1.56 \pm 0.34$	0.03747	3.83	$9.07 \pm 0.18$
3318	1.03	2	...	1.19	...	...	1.89	2	...	0.63	...	2.95	8.55
3439	0.89	2	...	0.97	...	...	1.44	2	...	0.24	...	3.28	8.50
3465	1.17	1	4.19	$1.24 \pm 0.36$	0.02898	445.8	1.72	2	...	0.38	...	3.51	$8.64 \pm 0.20$

**Note.** The full version of this table, including all columns and all 532 xCOLD GASS galaxies from Tables, 1, 3, and 4, is available online in a machine-readable FITS format. A detailed description of this table's contents, as well as the additional columns available online, is given in Section 2.5.

<sup>a</sup> Recommended CO-to-H<sub>2</sub> conversion factor calculated using the function of Accurso et al. (2017), in units of  $M_{\odot}(\text{K km s}^{-1} \text{ pc}^2)^{-1}$ .

**Table 4**  
Summary of APEX CO (2–1) Observations

ID	rms (mK)	$S_{\text{CO}2-1}$ (Jy km s <sup>-1</sup> )	$L'_{\text{CO}2-1}$ (10 <sup>8</sup> K km/s pc <sup>2</sup> )	S/N
11956	1.42	18.41	3.29	4.69
3189	2.06	...	...	...
3261	1.70	13.38	2.15	6.00
3519	1.72	18.92	3.96	4.60
3962	1.79	92.82	19.45	17.27
4030	1.54	24.18	6.72	8.88
4048	1.28	22.11	4.34	5.13
24183	1.53	65.52	13.81	14.68
41783	1.75	48.36	7.59	7.41
39548	1.65	20.05	2.75	5.33
10850	1.49	10.22	1.47	2.71
11223	1.43	129.87	18.75	26.25
11311	1.31	53.04	7.05	11.29
11295	1.94	50.70	9.20	6.38
11270	1.65	...	...	...
11845	1.69	67.08	10.12	12.30
1977	1.83	20.94	2.12	4.07
11019	1.74	...	...	...
11340	1.70	41.34	6.05	8.46
4045	1.82	106.86	8.54	43.81
3981	1.39	23.13	4.59	6.95
51276	2.50	34.01	3.39	5.24
56312	1.64	30.89	4.16	7.35
41869	1.91	...	...	...
31592	1.50	368.16	89.77	68.90
36169	2.14	225.42	57.33	26.85
109050	1.25	12.17	0.19	6.75
114072	1.53	...	...	...
122002	1.51	21.61	0.74	6.75
111047	2.87	...	...	...
123006	1.66	40.17	1.07	11.18
123010	3.89	129.87	3.18	14.84
114113	1.87	7.72	0.26	4.49
113141	1.40	13.57	0.27	4.79

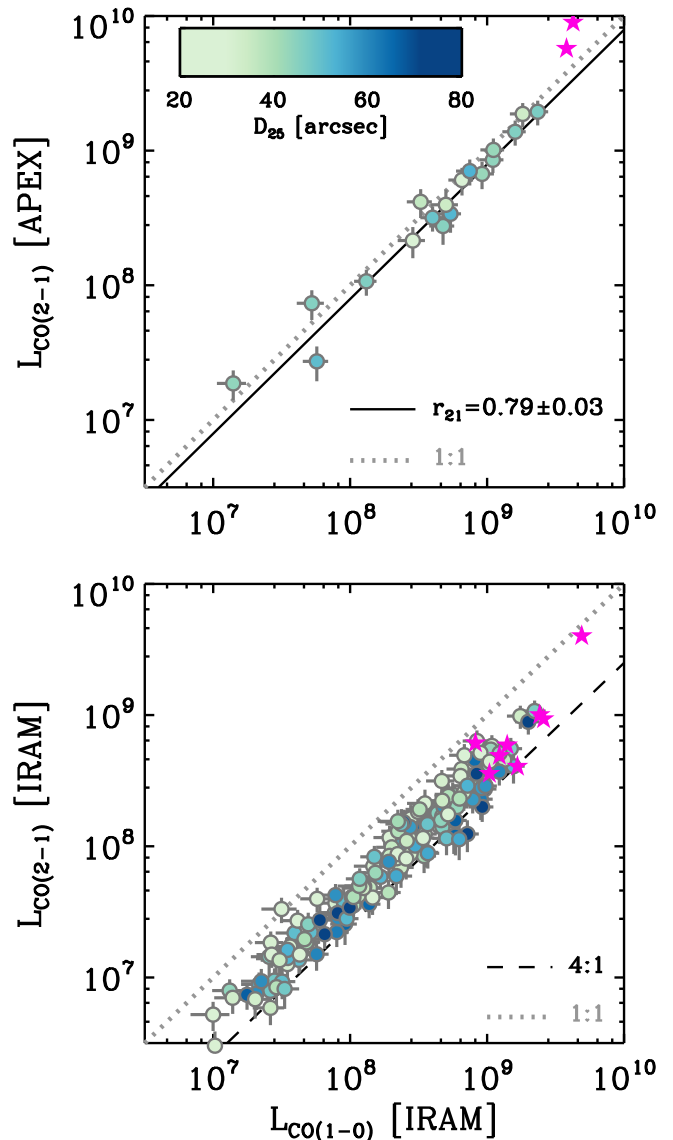
**Note.** The full version of this table, including all columns and all 532 xCOLD GASS galaxies from Tables 1, 3, and 4, is available online in a machine-readable FITS format.

$M_{\text{H}_2} = \alpha_{\text{CO}}(Z, \text{SSFR})L'_{\text{CO}(1-0), \text{cor}}$ . The error provided includes the uncertainty on the CO (1–0) line luminosity (see Column (8)) and the 35% uncertainty on the  $\alpha_{\text{CO}}$  conversion function as determined by Accurso et al. (2017). If FlagCO10 = 2 (see Column (3)), indicating a nondetection of the CO (1–0) line, then the value given is a  $3\sigma$  upper limit.

The full xCOLD GASS catalog, including all quantities presented in Tables 1 and 3, as well as all the IRAM CO spectra and SDSS images, can be retrieved from <http://www.star.ucl.ac.uk/xCOLDGASS>.

### 2.6. APEX CO (2–1) Observations

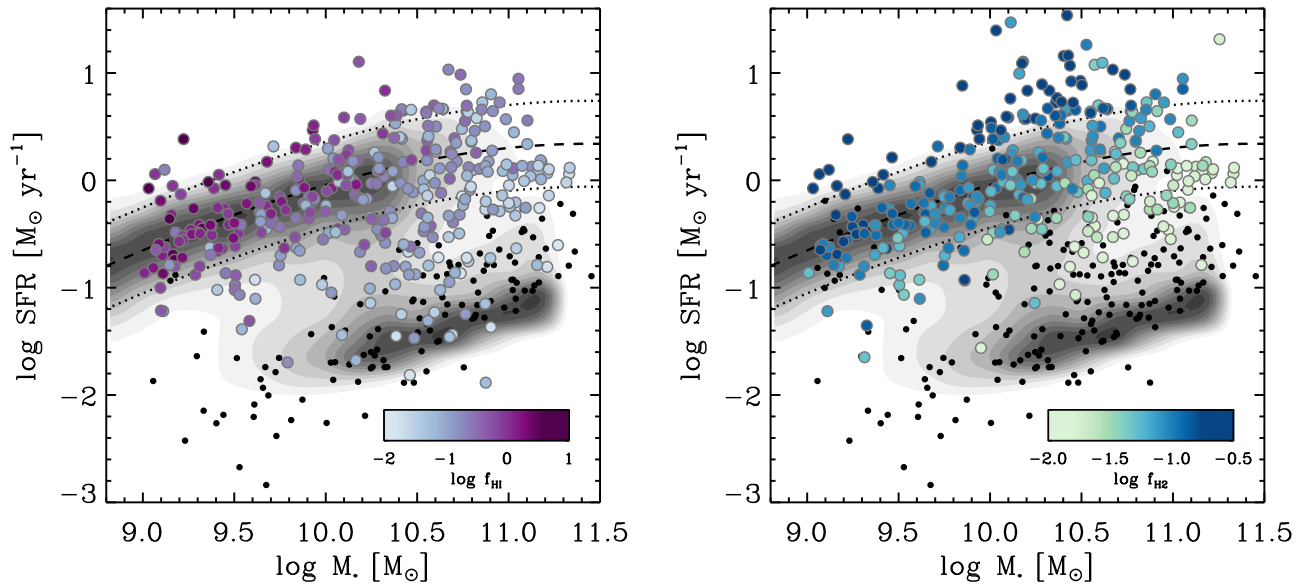
The CO (1–0) emission line is only one of the many tracers available to measure the mass of molecular gas in galaxies. At higher redshifts, it is more common to observe higher- $J$  transitions of this same molecule, as, for example, lines such as CO (2–1) and CO (3–2) fall into the 3 mm atmospheric window at  $z \sim 1$  and  $z \sim 3$ , respectively. Having both CO (1–0) and CO (2–1) observations for 68% of the xCOLD GASS sample, we would be in a good position to investigate how the



**Figure 7.** Relation between observed CO (1–0) and CO (2–1) line luminosities, with the former having been observed through the 27'' beam of the APEX telescope (top) or the 11'' beam of the IRAM telescope (bottom). In the top panel, the CO (1–0) luminosities have been corrected by a small aperture correction to account for the beam size difference, and the solid line shows the best-fitting value for  $r_{21}$ . In the bottom panel, the dotted line is the 1:1 relation, while the dashed line is a 4:1 relation. Galaxies are color-coded by their optical diameter, and the magenta stars represent merging systems.

luminosity ratio,  $r_{21} \equiv L_{\text{CO}(2-1)}/L_{\text{CO}(1-0)}$ , varies as a function of global galaxy properties. This is important, as a value of  $r_{21}$  has to be assumed to convert an observed CO (2–1) flux into  $M_{\text{H}_2}$ . However, the beam size difference implies that the IRAM CO (1–0) and (2–1) observations do not probe the same area of the galaxies; any galaxy-to-galaxy variations in the (2–1)/(1–0) ratio measured with IRAM could be due to either gas excitation variations or differences in the radial distribution of the gas.

To help disentangle these effects, we have obtained additional CO (2–1) data with the APEX telescope. With a beam size of 27'' at this frequency, these observations are a good match for the CO (1–0) fluxes measured with the IRAM 22'' beam. Observations were performed through the allocation of a total of 78 hr via both the ESO (proposal 091.B-0593) and Max-Planck channels. The APEX-1 receiver was used, tuned to the redshifted frequency of



**Figure 8.** Distribution of the xCOLD GASS sample in the SFR– $M_*$  plane, color-coded by atomic gas mass fraction (left) and molecular gas mass fraction (right). The smaller black symbols are galaxies undetected in the H I and CO (1–0) line, respectively. The grayscale contours show the overall SDSS population. The dashed and dotted lines indicate the position of the main sequence and the  $\pm 0.4\text{dex}$  scatter around this relation, respectively.

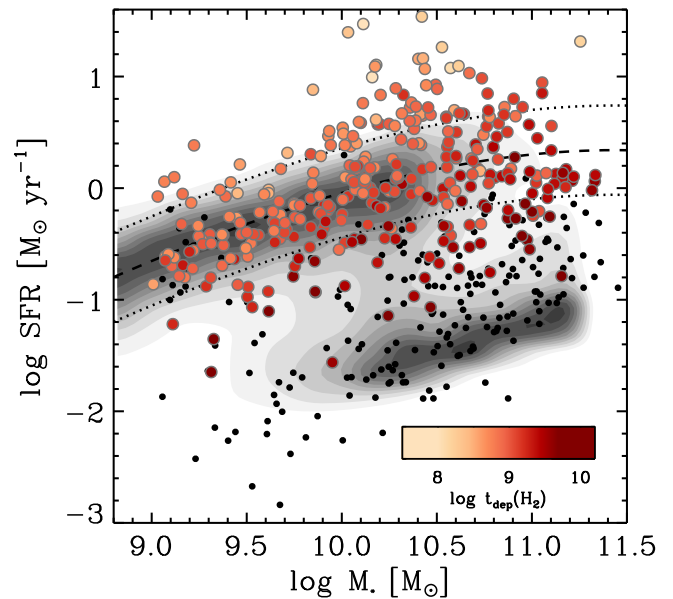
the CO (2–1) of each xCOLD GASS object, with a simple on-off observing mode. Integration times were set based on average observing conditions, rms noise requirements predicted from the measured IRAM CO (1–0), a standard value of  $r_{21} = 0.7$ , and a Galactic conversion factor. The detection rate ( $S/N > 4$ ) is 85%. The APEX data were reduced in CLASS using a procedure identical to that described above for the IRAM data. The reduced spectra for the 28 xCOLD GASS galaxies with an APEX CO (2–1) detection are shown in Figure 5, with measured line properties presented in Table 4.

### 3. Results

#### 3.1. The CO Luminosity Function

The CO luminosity function (LF) at  $z = 0$  is a useful tool, which xCOLD GASS is particularly well suited to calibrate. Commonly used calibrations of the CO LF were derived either using samples biased toward more extreme starburst galaxies (Keres et al. 2003; Obreschkow & Rawlings 2009) or indirectly using an empirical conversion between IR luminosities and CO line emission (Berta et al. 2013; Vallini et al. 2016). The xCOLD GASS sample, being only stellar mass selected, provides a unique opportunity to obtain a more complete and direct view of the CO LF at  $z = 0$ , as long as the completeness limits imposed by the stellar mass cutoff and the depth of the observations are taken into account.

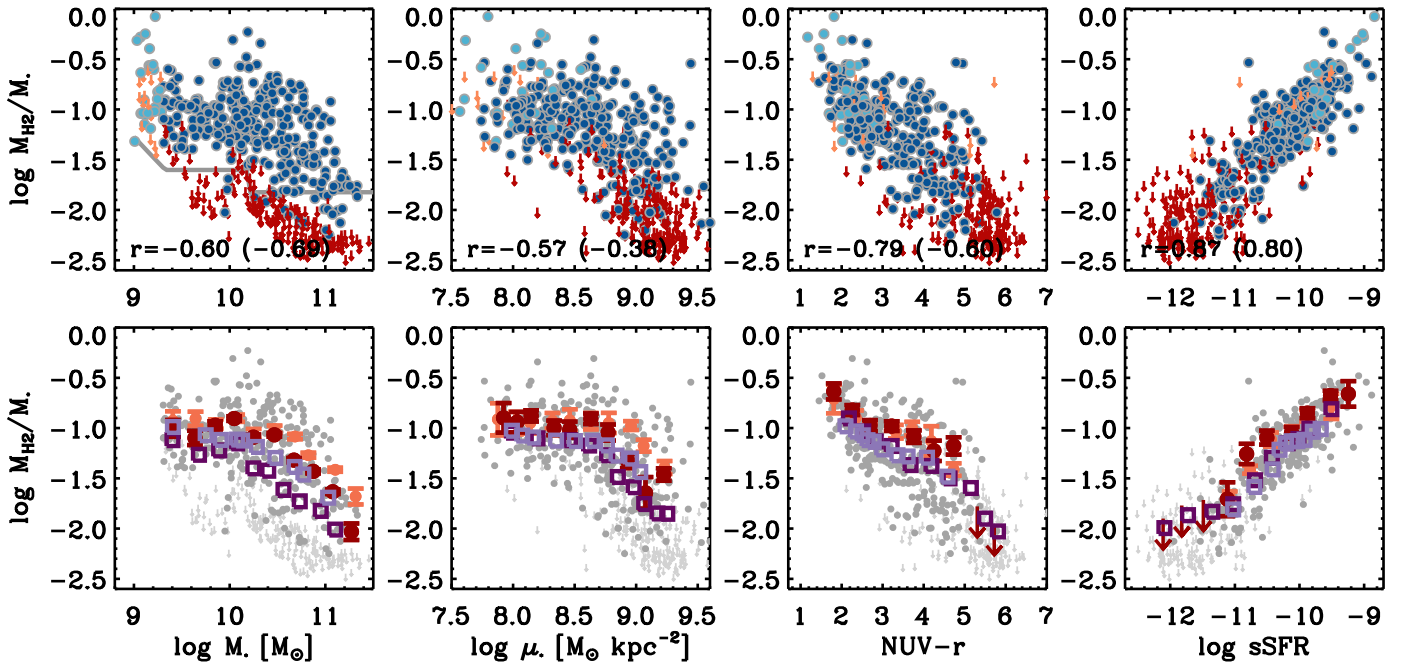
While the sample was selected to have a flat stellar mass distribution (see Figure 3), because it is extracted from a volume-limited parent sample, we only have to apply the statistical weights described in Section 2.2 to recover a complete luminosity function (LF). We note that we do not attempt here to correct for the contribution of galaxies with  $M_* < 10^9 M_\odot$ , and therefore we produce an LF that accounts for the contributions of galaxies more massive than  $10^9 M_\odot$ . However, given that there is a positive correlation between  $M_*$  and  $L'_{\text{CO}}$ , and given that the most CO-bright galaxies with  $M_* \sim 10^9 M_\odot$  have  $\log L'_{\text{CO}} < 7.5$ , it is highly unlikely that lower-mass galaxies contribute much if at all to the CO LF at  $\log L'_{\text{CO}} > 7.5$ . There is a second completeness



**Figure 9.** Distribution of the xCOLD GASS sample in the SFR– $M_*$  plane, color-coded by molecular gas depletion timescale. Symbols and lines as described in Figure 8.

limit to consider, caused by the xCOLD GASS observing strategy. Because the sample is gas fraction limited (i.e., the sensitivity limit is determined by the requirement to detect a fixed, constant gas mass fraction  $M_{\text{H}_2}/M_*$  in all the galaxies; see Section 2.4 and Figure 10), the depth in terms of CO luminosity varies by about an order of magnitude across the stellar mass range of the sample. At the highest-mass end of the sample, where the observations are shallowest in terms of CO luminosity, the gas fraction limit of the observations corresponds to  $\log L'_{\text{CO}} \sim 8.6$ .

The CO luminosity function for the xCOLD GASS sample is presented in Figure 6, with the estimated completeness limits due to stellar mass cut of the sample and the gas fraction integration limit shown by vertical lines at  $\log L'_{\text{CO}} \sim 7.5$  and



**Figure 10.** Molecular gas mass fraction as a function of stellar mass, stellar mass surface density, NUV- $r$  color, and specific SFR. Top row: all xCOLD GASS galaxies, with both CO detections (circles) and upper limits (arrows). Galaxies with  $\log M_* < 9.3$  where the upper limits are less constraining are shown in pale blue and orange, higher-mass galaxies in dark blue and red. The correlation coefficient between  $f_{\text{H}_2}$  and the  $x$ -axis parameter for the CO detections is given in each panel. Bottom row: mean  $f_{\text{H}_2}$  scaling relations obtained by stacking of all xCOLD GASS galaxies are shown with red circles, those for main-sequence galaxies only ( $|\Delta(\text{MS})| < 0.4$ ) as orange circles. The open squares show the weighted medians of  $\log f_{\text{H}_2}$  in bins of the  $x$ -axis parameter for all xCOLD GASS and main sequence only in dark and pale purple, respectively.

$\log L'_{\text{CO}} \sim 8.6$ , respectively. The xCOLD GASS CO LF was calculated using the statistical weights described in Section 2.2, making the sample volume-limited. To address the completeness issue caused by the fixed gas fraction integration limit, we produce two LFs by treating the upper limits differently: in one case we assign to the undetected galaxies their  $3\sigma$  upper limit on  $\log L'_{\text{CO}}$  (red symbols in Figure 6), and in the other we assign to them a value of  $\log L'_{\text{CO}} = 0$  (blue symbols). As expected, these two LFs are identical above the completeness limit of  $\log L'_{\text{CO}} \sim 8.6$ . The error on each point in the luminosity function was calculated using a bootstrap method. In this procedure, a randomly selected subsample of 80% of the full xCOLD GASS sample was selected, giving  $N$  galaxies. For each of these  $N$  galaxies, we assign a CO luminosity by randomly sampling a Gaussian centered around the measured CO luminosity of this galaxy and with a standard deviation corresponding to the  $1\sigma$  error. The CO LF for this subsample of  $N$  galaxies is then constructed, and this procedure is repeated  $N$  times. The final uncertainty on each data point in the LF determined from the full xCOLD GASS sample is the  $1\sigma$  distribution at the given luminosity within the  $N$  subsampled LFs produced by the bootstrap method. These are the points and errors shown in Figure 6, for both the methods of treating the nondetections.

Figure 6 illustrates that even in the  $L'_{\text{CO}}$  interval where the data are not affected by the stellar mass limit of the sample, the xCOLD GASS CO LF differs from the observed and empirically derived LFs from Keres et al. (2003) and Vallini et al. (2016), respectively. The knee of the xCOLD GASS CO LF is at larger  $L_{\text{CO}}$ , shifted downward in number density, and has a steeper slope. When the nondetections are assigned their  $3\sigma$  upper limits (red symbols), the faint-end slope appears to be

yet steeper. The true CO luminosity of many of these undetected galaxies is likely to be much lower than the  $3\sigma$  upper limits used here, and we therefore expect the “true” CO LF to lie somewhere between the functions determined with and without nondetections.

Finally, we fit the two xCOLD GASS CO luminosity functions with a Schechter function (Schechter 1976) over the luminosity interval where the stellar mass limit of the sample is not affecting the completeness ( $\log L_{\text{CO}} > 7.5$ ). The bootstrap errors on the individual points of the LFs are considered, and the covariance matrix is used to randomly sample the best-fit function. The best-fit Schechter functions to both LFs are shown in Figure 6, with the range of possible fits within the uncertainties illustrated by the red shaded area for the case where both CO detections and nondetections are considered. The parameters of the best-fit Schechter function for both cases are given in Table 5.

### 3.2. Gas Excitation

In Figure 7 the line luminosities of the CO (1–0) and CO (2–1) lines are compared. When measurements are made within the same aperture, there are very few galaxy-to-galaxy variations in the integrated  $r_{21}$  ratio. To achieve this comparison, we apply a small aperture correction to the IRAM CO (1–0) luminosities to account for the small difference in beam size with the APEX CO (2–1) measurements. These corrections, based on the technique described in Section 2.4, are in the range of 2%–10%.

Across the joint IRAM-APEX sample, the mean value of the luminosity ratio is  $r_{21} = 0.79 \pm 0.03$ . The linear scatter around this value is 0.23 and reduces to 0.15 if considering only galaxies with  $L_{\text{CO}(1-0)} > 10^8 \text{ K km s}^{-1} \text{ pc}^2$ . The xCOLD

**Table 5**  
Best-fit Schechter Function Parameters for the xCOLD GASS CO Luminosity Functions

	$\phi^*$ ( $\text{Mpc}^{-3}$ )	$L_{\text{CO}}^*$ ( $\text{K km s}^{-1} \text{pc}^2$ )	$\alpha$
Detections only	$(1.30 \pm 0.71) \times 10^{-3}$	$(7.00 \pm 1.88) \times 10^9$	$-1.13 \pm 0.05$
Detections+nondetections	$(9.84 \pm 5.41) \times 10^{-4}$	$(7.77 \pm 2.11) \times 10^9$	$-1.19 \pm 0.05$

GASS value of  $r_{21} \sim 0.8$  corresponds to an excitation temperature of 10 K, assuming that the gas is optically thick (Leroy et al. 2013). This value of  $r_{21}$  is slightly larger than the values of 0.5-0.7 reported from resolved observations of the disks of nearby star-forming spiral galaxies (e.g., Leroy et al. 2013; Rosolowsky et al. 2015). Higher values still of  $r_{21} \sim 1$  are usually reported for the nuclei of galaxies (e.g., Braine & Combes 1992; Sakamoto et al. 1995; Leroy et al. 2009). In Figure 7 we highlight the position of merging systems found within the xCOLD GASS data set. We may expect the gas in these systems to have higher excitation and/or to be more centrally concentrated as seen in some other nearby systems with detailed multitransition CO observations (e.g., Saito et al. 2017), although the physical conditions of the gas are likely a function of the specific geometry and evolution state of the merger (Ueda et al. 2012). While there are not enough merging systems within the xCOLD GASS sample to study these subtleties in detail, it makes an excellent comparison sample for observing programs specifically targeting such dynamically active systems.

### 3.3. Gas Fraction Scaling Relations

The distribution of the xCOLD GASS sample in the SFR- $M_*$  plane is presented in Figure 8. As expected, the detection rate of the CO line goes from nearly 100% for galaxies on and above the main sequence to zero for passive galaxies with very low SFRs. While individually undetected, using a spectral stacking technique, we measure in Saintonge et al. (2016) a mean ratio of molecular gas to stellar mass of 0.6% for the massive passive galaxies ( $M_* > 10^{10} M_\odot$ ,  $-12 < \log \text{SSFR} < -11$ ). Figures 8 and 9 also show how both molecular gas fraction ( $f_{\text{H}_2} \equiv M_{\text{H}_2}/M_*$ ) and depletion time ( $t_{\text{dep}}(\text{H}_2) \equiv M_{\text{H}_2}/\text{SFR}$ ) vary systematically in the SFR- $M_*$  plane. Galaxies above the main sequence have both higher gas fractions and shorter depletion times, while the reverse is true of galaxies below the main sequence. As pointed out already in Saintonge et al. (2016), it is the combination of variations in both gas contents and star formation efficiency that explains the position of galaxies in the SFR- $M_*$  plane. Figures 8 and 9 show that this trend extends to  $M_* < 10^{10} M_\odot$ .

To explore further the dependence of gas fractions on integrated galaxy properties, scaling relations for  $f_{\text{H}_2}$  are presented in Figure 10. The relation between  $f_{\text{H}_2}$  and  $M_*$  shows a mild dependence at  $M_* < 10^{10.5} M_\odot$  but a sharp drop-off afterward. This is in contrast with the atomic gas fractions,  $f_{\text{H I}}$ , which increase steadily as  $M_*$  decreases. Indeed, while the mean molecular-to-atomic ratio for massive galaxies is  $\langle R_{\text{mol}} \rangle \sim 0.35$ , it drops to only 0.1 for the lowest-mass galaxies in the sample (see also Catinella et al. 2017). The dependence of both  $f_{\text{H}_2}$  and the molecular ratio ( $R_{\text{mol}} \equiv M_{\text{H}_2}/M_{\text{H I}}$ ) on  $M_*$  in the xCOLD

GASS sample is qualitatively similar to those observed previously in the  $10^9$ - $10^{11.5} M_\odot$  stellar mass range by combining the COLD GASS data with CO observations from the Herschel Reference Survey (Boselli et al. 2014) and from ALLSMOG (Bothwell et al. 2014; Cicone et al. 2017). However, the xCOLD GASS scaling relations have the advantage of being based on a sample that is larger, deeper, and more homogeneous. The dependence of  $f_{\text{H}_2}$  on morphology (as parameterized here by the stellar mass surface density,  $\mu_*$ ) is similar, with gas fractions decreasing sharply when entering the regime of bulge-dominated galaxies ( $\log \mu_* \sim 8.7$ ).

The strongest correlations, however, are between  $f_{\text{H}_2}$  and quantities relating to SFR. While NUV- $r$  is a proxy for specific SFR (SSFR) since NUV color traces ongoing star formation and  $r$  band the older stellar population, the correlation with  $f_{\text{H}_2}$  is not as strong as with SSFR itself. The main difference between NUV- $r$  and SSFR is that the former does not consider dust obscuration, which explains the weaker correlation, as molecular gas is known to be best linked with dust-obscured star formation as measured in the mid- or far-infrared (e.g., Leroy et al. 2008).

To best compare these results with other studies and the results of models and simulations, we provide in Table 6  $f_{\text{H}_2}$  scaling relations measured in two different ways. The first method relies on a spectral stacking technique (Fabello et al. 2011; Saintonge et al. 2012, 2016) whose main advantage is to allow CO detections and nondetections to be combined fairly. The disadvantage is that the stacking process is linear by nature, whereas the distribution of  $f_{\text{H}_2}$  values in selected bins tends to be lognormal. The second method we use is to calculate weighted median values of  $\log f_{\text{H}_2}$  (we refer to this as the ‘‘binning method’’ in Table 6). This technique has the opposite pros and cons: it makes the better assumption that the distribution of  $f_{\text{H}_2}$  values in selected bins is lognormal, but it has to assume for the CO nondetections the value of  $f_{\text{H}_2}$  set by the upper limit. The latter is not a problem if there are few nondetections in any given bin and if the upper limits are well separated from the detections, but it becomes an issue when the rate of nondetections is significant. For both averaging methods, we also provide the  $f_{\text{H}_2}$  scaling relations for the complete xCOLD GASS sample, as well as for main-sequence galaxies only ( $|\Delta(\text{MS})| < 0.4$ ); readers are cautioned to select with care the optimal set of  $f_{\text{H}_2}$  scaling relations for their specific purposes.

For both methods, the errors reported include the statistical errors associated with the IRAM calibration and aperture corrections (which taken together are typically 20% for a given galaxy; see Saintonge et al. 2011a) and the sampling error determined from bootstrapping. This does not, however, include the systematic error on the conversion function,  $\alpha_{\text{CO}}$ , which Accurso et al. (2017) estimate to be 35%.

Throughout this work, we adopt the CO-to- $\text{H}_2$  conversion function of Accurso et al. (2017), which is primarily a function of

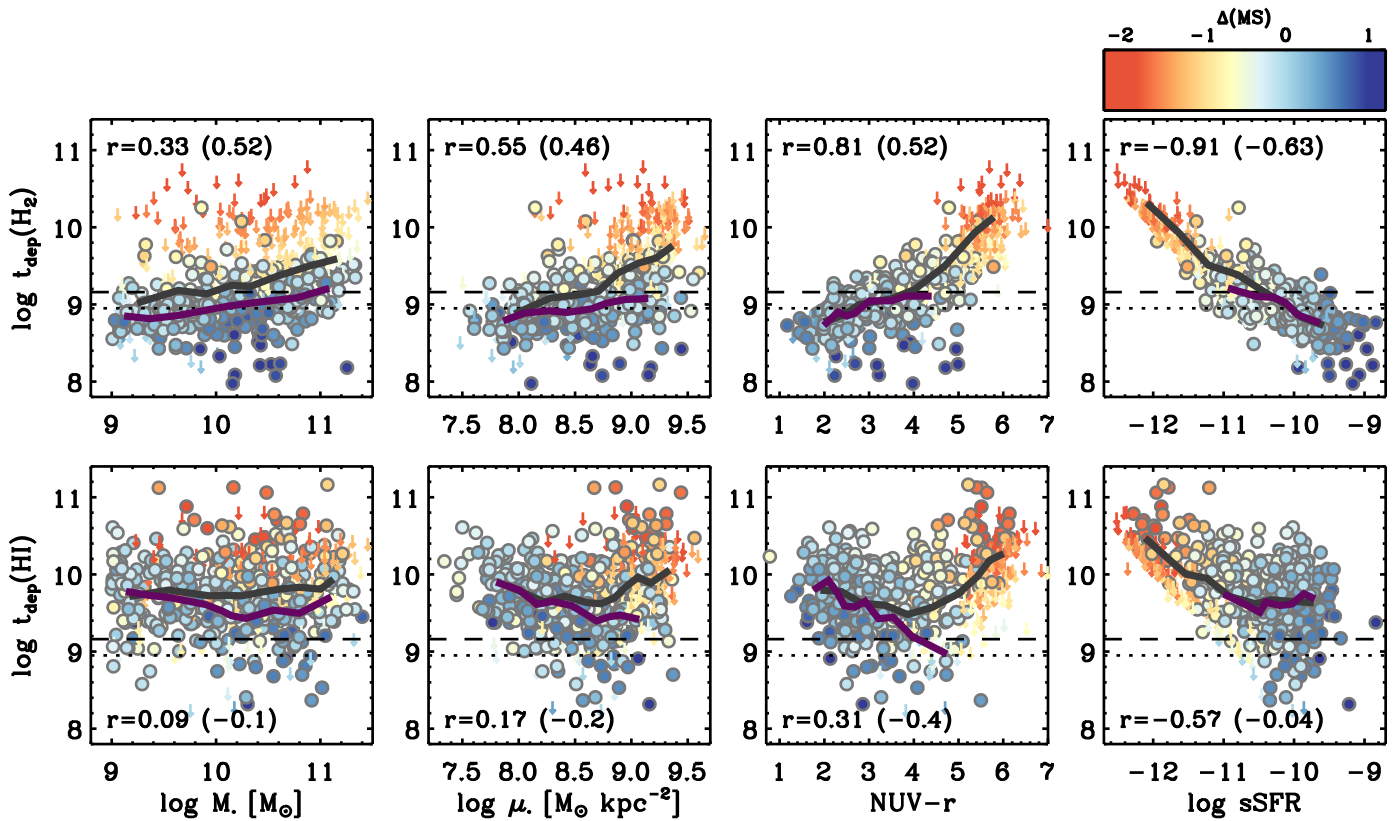
**Table 6**  
 $f_{\text{H}_2}$  Scaling Relations

All xCOLD GASS						Main Sequence Only					
Stacking			Binning			Stacking			Binning		
$\langle x \rangle$	$N$	$\log \langle f_{\text{H}_2} \rangle$	$\langle x \rangle$	$N$	$\langle \log f_{\text{H}_2} \rangle$	$\langle x \rangle$	$N$	$\log \langle f_{\text{H}_2} \rangle$	$\langle x \rangle$	$N$	$\langle \log f_{\text{H}_2} \rangle$
$x = \log M_*$											
9.407	36	$-1.01 \pm 0.041$	9.388	48	$-1.11 \pm 0.058$	9.406	23	$-0.93 \pm 0.049$	9.366	18	$-0.99 \pm 0.072$
9.638	34	$-1.08 \pm 0.035$	9.669	48	$-1.28 \pm 0.078$	9.643	19	$-0.89 \pm 0.033$	9.465	18	$-1.05 \pm 0.068$
9.848	41	$-0.97 \pm 0.020$	9.915	48	$-1.23 \pm 0.088$	9.854	24	$-0.96 \pm 0.023$	9.647	18	$-1.12 \pm 0.077$
10.04	61	$-0.90 \pm 0.011$	10.10	48	$-1.16 \pm 0.080$	10.07	26	$-0.89 \pm 0.017$	9.882	18	$-1.10 \pm 0.066$
10.24	66	$-1.08 \pm 0.013$	10.25	48	$-1.39 \pm 0.091$	10.25	22	$-1.05 \pm 0.023$	10.01	18	$-1.11 \pm 0.079$
10.46	70	$-1.05 \pm 0.009$	10.41	48	$-1.40 \pm 0.124$	10.46	16	$-0.99 \pm 0.018$	10.14	18	$-1.20 \pm 0.074$
10.67	63	$-1.34 \pm 0.011$	10.58	48	$-1.62 \pm 0.087$	10.68	20	$-1.10 \pm 0.014$	10.37	18	$-1.27 \pm 0.088$
10.87	56	$-1.41 \pm 0.009$	10.75	48	$-1.75 \pm 0.086$	10.82	21	$-1.26 \pm 0.013$	10.56	18	$-1.39 \pm 0.114$
11.07	48	$-1.66 \pm 0.012$	10.90	48	$-1.83 \pm 0.088$	11.10	17	$-1.41 \pm 0.010$	10.77	18	$-1.44 \pm 0.108$
11.27	15	$-2.02 \pm 0.041$	11.08	48	$-2.01 \pm 0.075$	11.31	5	$-1.68 \pm 0.039$	11.12	18	$-1.70 \pm 0.128$
$x = \log \mu_*$											
7.876	9	$-0.90 \pm 0.076$	8.025	42	$-1.03 \pm 0.049$	7.876	7	$-0.91 \pm 0.079$	7.976	17	$-1.04 \pm 0.093$
8.032	24	$-0.94 \pm 0.049$	8.211	42	$-1.09 \pm 0.068$	8.025	20	$-0.94 \pm 0.055$	8.117	17	$-1.05 \pm 0.068$
8.146	35	$-0.87 \pm 0.027$	8.427	42	$-1.10 \pm 0.058$	8.139	19	$-0.95 \pm 0.054$	8.257	17	$-1.09 \pm 0.072$
8.333	29	$-1.00 \pm 0.035$	8.589	42	$-1.16 \pm 0.097$	8.320	16	$-0.91 \pm 0.038$	8.431	17	$-1.11 \pm 0.074$
8.459	39	$-0.99 \pm 0.039$	8.709	42	$-1.26 \pm 0.114$	8.460	20	$-0.93 \pm 0.057$	8.509	17	$-1.13 \pm 0.071$
8.636	52	$-0.91 \pm 0.027$	8.850	42	$-1.49 \pm 0.124$	8.631	24	$-0.92 \pm 0.041$	8.682	17	$-1.12 \pm 0.089$
8.777	48	$-1.04 \pm 0.042$	8.962	42	$-1.60 \pm 0.080$	8.777	28	$-0.94 \pm 0.051$	8.764	17	$-1.15 \pm 0.084$
8.931	65	$-1.34 \pm 0.036$	9.044	42	$-1.68 \pm 0.113$	8.958	22	$-0.97 \pm 0.022$	8.810	17	$-1.27 \pm 0.162$
9.076	60	$-1.64 \pm 0.079$	9.135	42	$-1.84 \pm 0.062$	9.060	12	$-1.18 \pm 0.030$	8.956	17	$-1.32 \pm 0.110$
9.223	74	$-1.46 \pm 0.030$	9.229	42	$-1.84 \pm 0.092$	9.230	15	$-1.39 \pm 0.032$	9.060	17	$-1.42 \pm 0.121$
$x = \text{NUV}-r$											
...	0	...	2.140	46	$-0.90 \pm 0.057$	...	0	...	2.186	18	$-0.99 \pm 0.078$
1.807	16	$-0.64 \pm 0.042$	2.510	46	$-1.03 \pm 0.049$	1.809	5	$-0.71 \pm 0.069$	2.337	18	$-1.04 \pm 0.082$
2.260	54	$-0.82 \pm 0.025$	2.730	46	$-1.13 \pm 0.054$	2.347	36	$-0.89 \pm 0.036$	2.455	18	$-1.07 \pm 0.083$
2.690	72	$-0.96 \pm 0.025$	3.066	46	$-1.18 \pm 0.064$	2.690	57	$-0.99 \pm 0.031$	2.550	18	$-1.12 \pm 0.070$
3.220	54	$-0.97 \pm 0.023$	3.570	46	$-1.36 \pm 0.073$	3.320	35	$-1.02 \pm 0.033$	2.700	18	$-1.13 \pm 0.060$
3.760	54	$-1.09 \pm 0.031$	3.910	46	$-1.38 \pm 0.092$	3.720	25	$-0.98 \pm 0.033$	2.970	18	$-1.20 \pm 0.094$
4.250	44	$-1.22 \pm 0.050$	4.530	46	$-1.50 \pm 0.094$	4.186	18	$-1.15 \pm 0.081$	3.340	18	$-1.28 \pm 0.094$
4.730	47	$-1.16 \pm 0.041$	5.120	46	$-1.60 \pm 0.113$	4.730	13	$-1.42 \pm 0.031$	3.500	18	$-1.24 \pm 0.095$
5.305	56	$-1.78 \pm -9.00$	5.460	46	$-1.90 \pm 0.070$	...	2	...	4.006	18	$-1.29 \pm 0.089$
5.720	68	$-1.95 \pm -9.00$	5.790	46	$-2.03 \pm 0.049$	...	0	...	4.450	18	$-1.45 \pm 0.122$
$x = \log \text{SSFR}$											
-12.1	39	$-1.91 \pm -9.00$	-12.1	47	$-1.99 \pm 0.064$	...	0	...	-10.9	18	$-1.82 \pm 0.076$
-11.8	47	$-1.76 \pm -9.00$	-11.8	47	$-1.88 \pm 0.087$	...	0	...	-10.7	18	$-1.62 \pm 0.106$
-11.4	54	$-1.71 \pm -9.00$	-11.4	47	$-1.81 \pm 0.089$	...	0	...	-10.5	18	$-1.41 \pm 0.095$
-11.1	49	$-1.70 \pm 0.084$	-11.1	47	$-1.76 \pm 0.075$	-11.0	13	$-1.68 \pm 0.026$	-10.3	18	$-1.23 \pm 0.085$
-10.8	44	$-1.25 \pm 0.049$	-10.7	47	$-1.50 \pm 0.117$	-10.7	19	$-1.41 \pm 0.019$	-10.2	18	$-1.15 \pm 0.074$
-10.5	52	$-1.09 \pm 0.034$	-10.5	47	$-1.30 \pm 0.062$	-10.4	33	$-1.13 \pm 0.035$	-10.1	18	$-1.14 \pm 0.063$
-10.1	80	$-1.04 \pm 0.029$	-10.2	47	$-1.15 \pm 0.047$	-10.1	73	$-1.03 \pm 0.029$	-10.0	18	$-1.11 \pm 0.075$
-9.87	65	$-0.85 \pm 0.024$	-10.0	47	$-1.10 \pm 0.052$	-9.88	46	$-0.88 \pm 0.029$	-9.96	18	$-1.14 \pm 0.074$
-9.51	38	$-0.68 \pm 0.023$	-9.79	47	$-1.01 \pm 0.047$	-9.50	8	$-0.77 \pm 0.062$	-9.87	18	$-1.04 \pm 0.076$
-9.24	7	$-0.66 \pm 0.064$	-9.49	47	$-0.81 \pm 0.057$	...	0	...	-9.66	18	$-1.00 \pm 0.070$

metallicity, with a secondary dependence on the offset of the galaxy from the star formation main sequence. In that work (see their Figures 8 and 9), we show that were we to use a constant Galactic conversion factor across the xCOLD GASS sample, the scatter around key scaling relations for  $f_{\text{H}_2}$  and the depletion timescale would increase. Tacconi et al. (2017) also show the impact of using different prescriptions for the CO-to- $\text{H}_2$  conversion function on molecular gas scaling relations, combining xCOLD GASS with a sample of high-redshift galaxies.

### 3.4. Depletion Time Scaling Relations

In previous studies, we have reported systematic variations of the molecular gas depletion time,  $t_{\text{dep}}(\text{H}_2) = M_{\text{H}_2}/\text{SFR}$ , across the galaxy populations (Saintonge et al. 2011b, 2012, 2016; Genzel et al. 2015; Tacconi et al. 2017). These variations have been associated with dynamical effects that can increase or decrease the pressure within the ISM, thus influencing how much of the cold molecular gas can reach the high densities of prestellar cores. The story is different for



**Figure 11.** Comparison between depletion timescales for molecular (top row) and atomic gas (bottom row) and  $M_*$ , stellar mass surface density, NUV- $r$ , and SSFR. Galaxies are color-coded by their offset from the main sequence,  $\Delta(\text{MS})$ . Weighted medians in bins of the  $x$ -axis parameter are given including all galaxies in the xCOLD GASS/xGASS samples. In each panel, the correlation coefficient is given for all galaxies (and main-sequence galaxies only), while the dashed line shows the weighted median value of  $\log t_{\text{dep}}(\text{H}_2)$  across the entire sample and the dotted line is the median value for main-sequence galaxies only.

the atomic gas depletion time,  $t_{\text{dep}}(\text{H I}) = M_{\text{H I}}/\text{SFR}$ , which has been measured to have much larger galaxy-to-galaxy variations, but no systematic dependence on global galaxy properties (Schiminovich et al. 2010). Here we revisit these results, but now expanding the analysis to  $M_* < 10^{10} M_{\odot}$ , as made possible by xCOLD GASS and xGASS.

Figure 11 shows how both  $t_{\text{dep}}(\text{H}_2)$  and  $t_{\text{dep}}(\text{H I})$  vary as a function of integrated properties. It confirms previous observations that  $t_{\text{dep}}(\text{H I})$  is independent of  $M_*$  and at fixed mass has larger scatter than  $t_{\text{dep}}(\text{H}_2)$ . When looking at main-sequence galaxies, the weighted mean values and scatter are  $\langle \log t_{\text{dep}}(\text{H}_2) \rangle = 8.98 \pm 0.27$  and  $\langle \log t_{\text{dep}}(\text{H I}) \rangle = 9.65 \pm 0.44$ . The longest molecular gas depletion times we measure are  $< 10^{10}$  yr, while atomic gas depletion times can be in excess of  $10^{11}$  yr. This illustrates clearly how galaxies may have large reservoirs of cold atomic gas that are not associated with the star formation process, as may be the case, for example, in early-type galaxies (Serra et al. 2011, 2014; Geréb et al. 2016) and in low-mass galaxies.

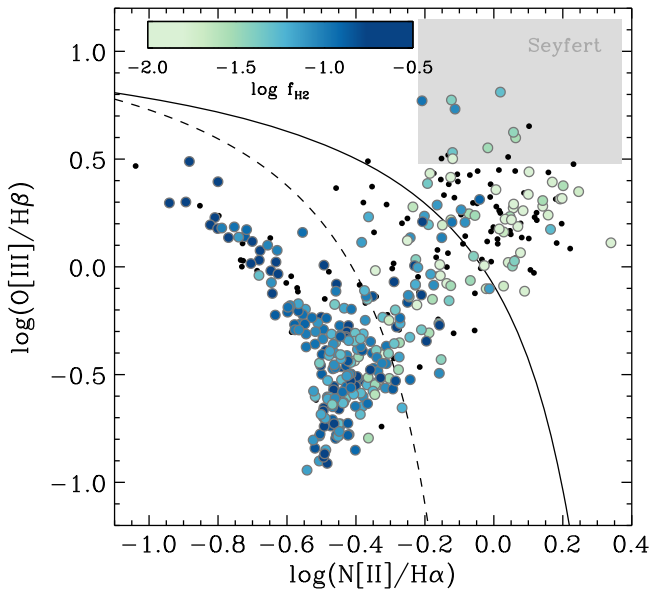
### 3.5. Molecular Gas in AGN Hosts

Gas offers a possible explanation for the observed correlation between supermassive black hole mass and the properties of its host galaxy (e.g., bulge mass and stellar velocity dispersion; Magorrian et al. 1998; Häring & Rix 2004; Merloni et al. 2010). The correlation can be expected under the assumption that both host galaxy and supermassive black hole grow together through merging and as a function of the

availability of gas. Evidence for this fundamental link between black hole and galaxy growth includes the remarkable similarity between the redshift evolution of star formation activity (i.e., the Lilly–Madau diagram) and that of the rate of accretion onto supermassive black holes (e.g., Boyle & Terlevich 1998; Aird et al. 2010; Merloni & Heinz 2013). Under this scenario, one would expect a *positive* correlation between the molecular gas fraction of galaxies and incidence of AGN activity.

On the other hand, the ability of AGNs to drive massive molecular gas outflows (Sturm et al. 2011; Ciccone et al. 2014; Costa et al. 2014) suggests a different scenario for the link between molecular gas and AGN activity. Feedback from AGNs is an appealing quenching mechanism, as it can explain why most quenched galaxies are bulge dominated (Bell 2008; Somerville et al. 2008). If the AGN-driven molecular outflows are indeed an important quenching agent, then we would expect a *negative* correlation between AGN activity and the molecular gas content of galaxies. Whether the observations are consistent with either of these scenarios depends not only on the physical mechanisms at play but perhaps mostly on the timescales involved in the various transformations.

What is then the observed link between the molecular gas contents of galaxies and AGN activity? In Figure 12 we show the distribution of the xCOLD GASS sample in the BPT diagram (Baldwin et al. 1981), with the color-coding representing the molecular gas mass fraction,  $f_{\text{H}_2}$ . Visual inspection suggests that galaxies in the AGN part of the BPT diagram tend to be gas-poor, with low gas fractions and a



**Figure 12.** Distribution of the xCOLD GASS galaxies in the BPT diagram. Shown are the galaxies with  $S/N > 3$  in the SDSS spectrum in all four emission lines. Galaxies are color-coded by their molecular gas mass fractions, with CO nondetections shown as the smaller black symbols. The empirical relation of Kauffmann et al. (2003) and the theoretical relation of Kewley et al. (2001) to separate systems where gas is ionized by star formation and AGN activity are shown as the dashed and solid lines, respectively. The gray shaded regions shows the locus of Seyfert galaxies.

higher rate of nondetection, but gas fractions possibly increasing back in Seyfert galaxies, especially those with the highest  $[O III]/H\beta$  line ratios. However, to properly assess whether active and inactive galaxies differ in terms of their molecular gas content, we must control for SSFR, given the strong correlation with  $f_{H_2}$  (see Figure 10). After extracting samples of active and inactive galaxies matched in SSFR from the high-mass COLD GASS sample ( $M_* > 10^{10} M_\odot$ ), the K-S statistics reveal with a test probability of 0.12 that BPT-selected AGN hosts have gas fractions slightly lower than matched xCOLD GASS inactive galaxies (1.4% and 2.1%, respectively). The test was done considering both CO detections and nondetection. However, if focusing only on the Seyfert subsample, the test reveals that they are indistinguishable from the matched inactive control sample in terms of molecular gas fraction, though with only a handful of Seyferts in the xCOLD GASS sample, the statistics are poor.

The slightly below average molecular gas content of AGN hosts is consistent with the analysis of Shimizu et al. (2015), which showed that the AGNs in COLD GASS and in the *Swift*/BAT sample tend to lie below the main sequence, where we have shown gas fractions to decrease (Figure 8). The analysis of Shimizu et al. (2015) also reveals that, on the other hand, the brightest AGNs tend to be in high-mass star-forming galaxies with a high merger rate (see also Koss et al. 2011). While the xCOLD GASS sample only contains a handful of these bright AGNs, they do appear to have higher gas fractions than weaker AGNs and on par with SSFR-matched inactive galaxies.

By targeting more nearby moderately luminous Seyferts from the LLAMA survey with APEX and JCMT, Rosario et al. (2017, submitted) were able to study the possible impact of AGNs on molecular gas in the central regions, where the influence of the AGNs (if any) should be greatest. They report central gas fractions and star formation efficiencies that are

similar between active and matched control inactive galaxies, which suggests that nuclear radiation does not couple efficiently with the surrounding molecular gas. Kirkpatrick et al. (2014) also find no impact of AGNs on star formation efficiency in galaxies from the 5MUSES sample.

Coming back to the two scenarios described at the beginning of this section, the xCOLD GASS results tentatively suggest that the correlation between molecular gas and AGN activity is a function of AGN strength; normal or elevated molecular gas contents sustain fueling onto Seyfert nuclei, while the hosts of weaker AGNs show depletion of their molecular gas reservoirs, possibly after a period of more intense activity and feedback. Observations of molecular line emission in large, complete samples of galaxies hosting AGNs with a wide range of luminosities will be key to further disentangling the competing effects of fueling and feedback.

## 4. Discussion

### 4.1. From Circumgalactic Gas to Star-forming Regions

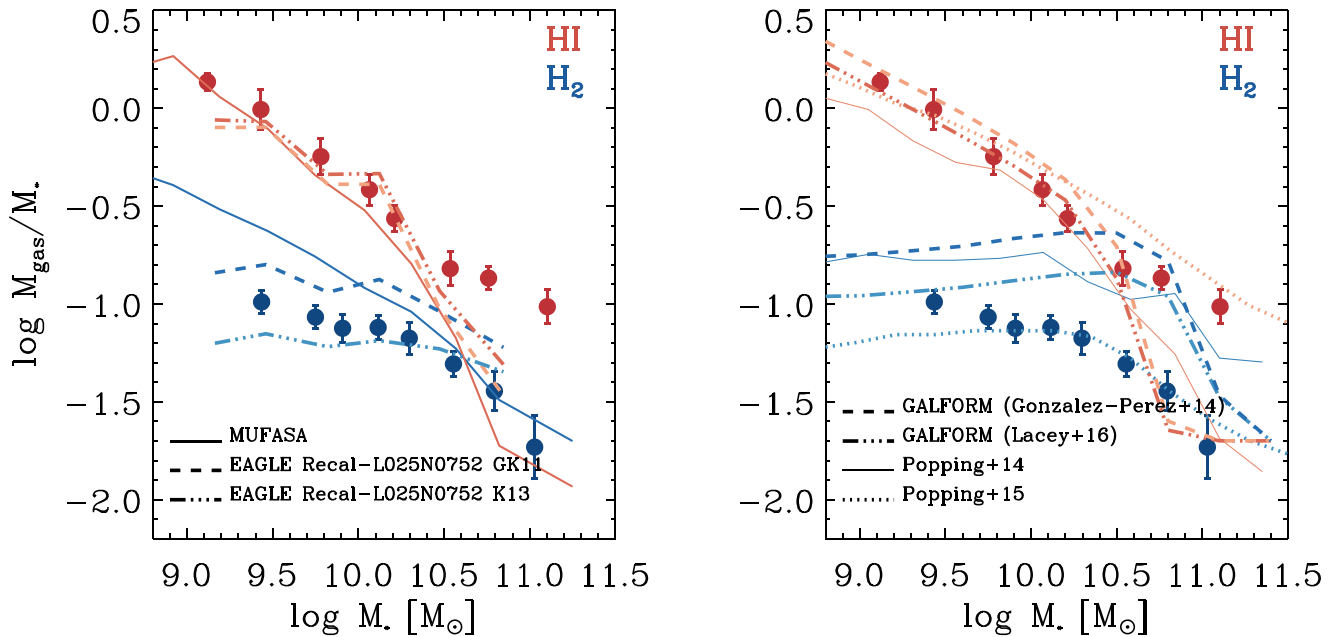
There is significant diagnostic power in the cold gas contents of galaxies. For example, identifying whether galaxies are quiescent because they are gas-poor or because they are very inefficient at converting any cold gas they may have into stars leads to vastly different interpretations as to the mechanisms responsible for quenching. The xCOLD GASS view on this is that the availability of molecular gas is mostly responsible for determining the SFR of a galaxy ( $f_{H_2}$  correlates strongly with SSFR; Figure 10). However, the data show that the depletion timescale of the molecular gas also correlates with star formation activity (Figure 11). The COLD GASS-low sample allows us here to extend the conclusions of Saintonge et al. (2016) that, on average, the SSFR of galaxies is set by both the molecular gas fraction and the star formation efficiency.

Having established this, the questions now become (1) what sets the molecular gas fraction of a galaxy and (2) why does the molecular gas depletion time vary across the local galaxy population. To address these questions, we need to look on scales much larger and much smaller than the molecular disks of the xCOLD GASS galaxies.

For the first question, it is helpful to consider the broader galactic ecosystem. Using the Cosmic Origins Spectrograph on *HST*, the circumgalactic medium (CGM) of galaxies from GASS was probed via absorption features in the spectra of background quasars. Borthakur et al. (2015) report a significant correlation between  $Ly\alpha$  equivalent width in the CGM and  $f_{H I}$  in the ISM. This correlation is even stronger than the correlation between  $Ly\alpha$  equivalent width and the SSFR, a result consistent with our observation in Figure 11 that H I is less tightly connected to star formation than  $H_2$ . This implies a physical connection between the atomic gas in the ISM of galaxies and their CGM, bridging the significant scale difference between the two components, and consistent with a picture where the cold atomic gas reservoir of galaxies is fed by accretion of gas from the CGM (Borthakur et al. 2015).

The next step in the journey of gas from CGM to stars is the conversion of atomic gas to the molecular phase. How the molecular ratio,  $R_{mol} \equiv M_{H_2}/M_{H I}$ , varies across the xCOLD GASS sample is studied in detail in Catinella et al. (2017), but as can be seen in Figures 11 and 13, the global atomic and molecular gas masses of galaxies relate differently to SFR and  $M_*$  across the sample. For example, the highest values of  $R_{mol}$





**Figure 13.** Molecular and atomic gas fraction dependence on  $M_*$ , from xGASS/xCOLD GASS, compared with model predictions. Left: comparison with the hydrodynamic simulations MUFASA (Davé et al. 2017) and EAGLE (Lagos et al. 2015; Crain et al. 2017). The two EAGLE models differ in the prescription used to predict how much of the total cold gas is molecular. Right: comparison with semianalytical models, two different versions of GALFORM (Gonzalez-Perez et al. 2014; Lacey et al. 2016), and the work of Popping et al. (2014) and Popping et al. (2015).

are observed in galaxies with high stellar masses, particularly at high SFRs (Saintonge et al. 2016), and while  $R_{\text{mol}} \sim 0.3$  in galaxies with  $M_* > 10^{10} M_\odot$  (Saintonge et al. 2011a), the ratio plummets to a mean value of  $\sim 0.1$  in galaxies with  $M_* < 10^{10} M_\odot$  (Catinella et al. 2017).

Forming molecular gas clouds with  $T \sim 20$  K and densities of  $\sim 10^3 \text{ cm}^{-3}$ , the conditions of the gas probed by our CO (1–0) observations, appears to be a necessary but not sufficient condition for star formation to efficiently proceed. Molecular gas traced by CO (1–0) may be too diffuse to lead to star formation, and we have previously hypothesized that “contamination” from this diffuse molecular gas may be the reason we observe variations in  $t_{\text{dep}}(\text{H}_2)$  across the COLD GASS sample (Saintonge et al. 2011b), based on several studies that have shown how SFR correlates more tightly and linearly with the luminosity of molecular lines with higher critical densities than CO (1–0), such as HCN (1–0) (e.g., Gao & Solomon 2004; Graciá-Carpio et al. 2006; García-Burillo et al. 2012). While these pioneering studies mostly targeted intensely star-forming, infrared-bright galaxies, recent instrumentation improvements have allowed two important breakthroughs: the observation of molecular lines such as HCN and  $\text{HCO}^+$  (1–0) in main-sequence star-forming galaxies and even early-type galaxies (Crocker et al. 2012), and the mapping of these lines at kiloparsec scales rather than integrated over entire galaxies. The latter is particularly important to link the global, statistical studies with high-resolution observations of individual clouds in the Milky Way and other very nearby galaxies (Wu et al. 2005; Buchbender et al. 2013).

A very exciting recent turn of events in the field of star formation studies is the realization that the systematic variations in star formation efficiency across the galaxy population first revealed by COLD GASS trickle down to small scales. For example, Usero et al. (2015) show that the dense gas fraction depends strongly on local conditions within the disk of a galaxy, and by focusing on M51, Bigiel et al.

(2016) reveal that spatial variations in star formation efficiency and dense gas fraction are associated with the local environment, and in particular pressure conditions. Even more interestingly, Hughes et al. (2013, 2016) show that it is the properties of GMCs themselves that vary not only as a function of local environment but also with the global properties of galaxies (their total  $M_*$  or gas surface density, for example).

The systematic observations of molecular gas throughout the local galaxy population with xCOLD GASS have helped to uncover this vast multiscale relation between the CGM, the atomic ISM, the cold molecular gas, and the star formation process on small scales. This complex chain of correlations between the properties of the CGM down to star formation efficiency at the smallest of scales suggests that “whole cloud” theories for star formation (e.g., Krumholz & McKee 2005; Federrath & Klessen 2012) may have to also take into account the larger-scale environment that regulates the availability of gas on small scales.

#### 4.2. The Importance of Cold Gas Scaling Relations for Galaxy Formation Simulations

The cold gas scaling relations also have strong constraining power for cosmological simulations. For example, since simulations and models typically use the empirical constraint of the  $z = 0$  stellar mass function to tune their parameters, it leaves the gas mass function as a powerful reference to ex post facto assess their predictive power. To illustrate this, we show in Figure 13 how the xCOLD GASS scaling relations between molecular and atomic gas fractions and  $M_*$  compare to the results of semianalytical and hydrodynamical models. The most recent generation of large hydrodynamical simulations such as EAGLE, ILLUSTRIS, and MUFASA can track the cold ( $T < 10^4$  K) ISM of galaxies, but to further separate this cold component between the atomic and molecular phases, one of many possible “subgrid” recipes must be applied. These

prescriptions are both theoretical and empirical in nature and depend on quantities such as metallicity, dust-to-gas ratio, radiation field strength, and pressure (e.g., Blitz & Rosolowsky 2006; Krumholz et al. 2009; Gnedin & Kravtsov 2011; Krumholz 2013).

For the EAGLE simulation (Crain et al. 2015; Schaye et al. 2015; McAlpine et al. 2016), Lagos et al. (2015) implement the recipes of Gnedin & Kravtsov (2011) and Krumholz (2013); both have a dependence on the radiation field and the amount of metals in the ISM, but the latter has an additional dependence on the atomic gas column density. Comparison with the accurate xCOLD GASS data points shows that neither recipe is particularly successful in predicting the correct amount of molecular gas in galaxies with  $\log M_*/M_\odot < 10.5$ , with the Krumholz (2013) prescription marginally preferred. MUFASA computes the molecular gas mass fractions on the fly using a recipe based on Krumholz et al. (2009), which results in good agreement with HI gas fractions at the low-mass end and H<sub>2</sub> gas mass fractions for more massive galaxies, but it overpredicts the molecular gas content of low-mass galaxies. This in part arises owing to MUFASA’s prescription that adds a subgrid clumping factor to Krumholz et al. (2009) to aid the resolution convergence of SFRs, which for relatively low resolution simulations such as MUFASA ends up yielding an increased molecular gas content. As with the EAGLE comparison using two different H<sub>2</sub> formation recipes, this illustrates that detailed assumptions regarding the subgrid ISM model can significantly alter the predicted H<sub>2</sub> and HI content of simulated galaxies. Hence, while the gas content is emerging as a powerful constraint on models, which physical processes it actually constrains remains unclear owing to the significant differences in predictions between subgrid models even when using the same underlying simulation. A feature shared by all the hydrodynamic simulations investigated in Figure 13 is that they robustly predict the atomic gas mass fraction in galaxies with  $\log M_*/M_\odot > 10.5$  but do not produce enough cold atomic gas in the most massive galaxies. This result highlights how the predicted HI gas fractions are far less dependent on the specific subgrid atomic-to-molecular conversion prescription applied, but that massive gas-rich galaxies are not successfully produced.

Similarly, semianalytic models are consistently reproducing very well the HI contents of galaxies with  $\log M_*/M_\odot < 10$ . The one simulation shown in Figure 13 that does the best at reproducing both molecular and atomic gas fraction scaling relations over the entire stellar mass range probed by xCOLD GASS is that of Popping et al. (2015). This semiempirical model, however, also stands apart as having used the molecular and atomic gas scaling relations as a constraint. Of particular note is the overestimation of the molecular gas fractions in all the other semianalytic models presented in Figure 13. As star formation is linked with the molecular phase, the fact that these simulations reproduce well the  $z = 0$  stellar mass function but not the  $f_{\text{H}_2}$  scaling relation suggests that their detailed star formation histories may not be accurate. Whether they are used as a test of the output of simulations (e.g., Lagos et al. 2015; Lacey et al. 2016; Davé et al. 2017) or as fitting constraints (e.g., Popping et al. 2015; Martindale et al. 2016), the cold gas scaling relations, which have been observed and calibrated up to  $z \sim 2$  (Tacconi et al. 2017), offer significant opportunities to refine galaxy formation models and in particular to constrain

subgrid recipes, which are currently a significant source of uncertainty.

## 5. Conclusions

The important role of the gas cycle in the galaxy evolution framework is increasingly obvious, through observations of line and continuum emission in high-redshift galaxies, as well as modeling and simulation work. The range of scales involved in this gas cycle is enormous: from  $> \text{Mpc}$  scales for the large but diffuse and hot gas reservoirs in the intergalactic medium, down through the CGM and ISM, and to scales smaller than a parsec where star formation is taking place.

We presented here the full and final data release of xCOLD GASS, the combination of two IRAM 30 m large programs: the original COLD GASS (Saintonge et al. 2011a), which targeted galaxies with  $M_* > 10^{10} M_\odot$ , and its extension COLD GASS-low, adding galaxies in the mass range  $10^9\text{--}10^{10} M_\odot$ . The xCOLD GASS “survey philosophy” can be summarized by the following key points:

1. Unbiased sample selection: to derive accurate and representative scaling relations between gas and global galaxy properties, a representative and unbiased sample is of the utmost importance. xCOLD GASS stands apart from previous large CO surveys (e.g., Sanders & Mirabel 1985; Kenney & Young 1989; Braine et al. 1993; Sage 1993; Young et al. 1995; Boselli et al. 1997; Lisenfeld et al. 2011; Young et al. 2011), as it does not target galaxies in specific environments, or with particular morphologies or rates of star formation. The sample selection based only on stellar mass and redshift out of the SDSS DR7 spectroscopic sample makes possible the derivation of robust and representative scaling relations.
2. Large sample size with dynamic range: the sample size of 532 galaxies is key, as with it we can define both mean scaling relations and the scatter about the mean, as well as examine multiparameter dependences. Furthermore, the flat stellar mass distribution (see Figure 3) ensures a large dynamic range for all the physical properties under consideration (e.g.,  $M_*$ , SFR, metallicity) while preserving the statistical relevance of the sample.
3. Homogeneous and accurate measurements: all the physical properties provided as part of the survey have been measured across the sample using the same quality data products and the same methods. This was done for both the molecular gas measurements themselves, all derived from consistent IRAM 30 m observations, and the quantities measured from the ancillary multiwavelength data sets (SDSS, WISE, GALEX, etc.).
4. Consistent observing strategy: by using a rigorous observing strategy, we can provide some meaningful and constraining upper limits on CO line fluxes for all the galaxies where line emission is not detected. This is essential to derive scaling relations for the entire galaxy population.

By adding the COLD GASS-low component to the original survey, thus forming xCOLD GASS, we have been able to extend our systematic investigation of the molecular gas contents of the local galaxy population to systems with stellar masses as low as  $10^9 M_\odot$  with the following key results:







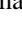

1. The molecular gas mass fraction,  $f_{\text{H}_2} = M_{\text{H}_2}/M_*$ , is on average 10% in galaxies with  $M_* < 5 \times 10^{10} M_\odot$  and then plummets rapidly to 1% as  $M_*$  increases to  $10^{11} M_\odot$ . There is a direct link between this scaling of  $f_{\text{H}_2}$  with  $M_*$  and the shape of the main sequence in the SFR- $M_*$  plane.
2. The strongest dependence of  $f_{\text{H}_2}$  is on quantities tracking star formation, in particular SSFR, where the correlation coefficient is  $r = 0.82$ . While strong ( $r = -0.63$ ), the correlation is weaker with NUV- $r$  color; unlike SSFR, this quantity is not corrected for dust extinction, showing how molecular gas and dust-obscured star formation are strongly linked.
3. By using the CO-to- $\text{H}_2$  conversion function of Accurso et al. (2017), which is calibrated independently of any assumption on the relation between molecular gas and SFR, we are able to show that while star formation efficiency varies systematically across the galaxy population, stellar mass is not the key parameter driving these variations.
4. Through complementary observations of the CO (2-1) line with the APEX telescope, we derive a value of  $r_{21} = 0.79 \pm 0.03$  for the (2-1)/(1-0) CO luminosity ratio. This value is applicable for observations that, as in the case of xCOLD GASS, integrate over the entire ISM of galaxies, and it is intermediate between values typically measured in the central and outer regions of nearby star-forming galaxies.
5. The atomic and molecular gas mass fraction scaling relations have strong constraining power for galaxy formation models. We show that modern hydrodynamic and semianalytic simulations, which all reproduce well the  $z = 0$  stellar mass function, do not succeed as well in reproducing the cold gas scaling relations, unless those gas relations are used as constraints.





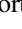
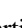
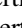
All the members of the xCOLD GASS team wish to warmly thank the staff at the IRAM observatory for the continuous help and support throughout the 6 yr over which observations for the two large programs were conducted. This study is also based on observations collected at the European Southern Observatory, Chile (proposal no. 091.B-0593).

We also thank Claudia Lagos and Gergő Popping for making the results of their simulations available and for discussing their specifics, and we thank Taro Schimizu and Mike Koss for discussions on the question of molecular gas in AGN hosts.

A.S. acknowledges support from the Royal Society through the award of a University Research Fellowship. B.C., L.C., and S.J. acknowledge support from the Australian Research Council's Discovery Project funding scheme (DP150101734). B.C. is the recipient of an Australian Research Council Future Fellowship (FT120100660).

#### ORCID iDs

Amélie Saintonge  <https://orcid.org/0000-0003-4357-3450>  
 Barbara Catinella  <https://orcid.org/0000-0002-7625-562X>  
 Linda J. Tacconi  <https://orcid.org/0000-0002-1485-9401>  
 Reinhard Genzel  <https://orcid.org/0000-0002-2767-9653>  
 Luca Cortese  <https://orcid.org/0000-0002-7422-9823>  
 Thomas J. Fletcher  <https://orcid.org/0000-0002-1633-1117>  
 Timothy M. Heckman  <https://orcid.org/0000-0001-6670-6370>  
 Steven Janowiecki  <https://orcid.org/0000-0001-9165-8905>

Katharina Lutz  <https://orcid.org/0000-0002-6616-7554>  
 David Rosario  <https://orcid.org/0000-0002-0001-3587>  
 Jing Wang  <https://orcid.org/0000-0002-6880-4481>  
 Stijn Wuyts  <https://orcid.org/0000-0003-3735-1931>  
 Sanchayeeta Borthakur  <https://orcid.org/0000-0002-2724-8298>  
 Isabella Lamperti  <https://orcid.org/0000-0003-3336-5498>  
 Guido W. Roberts-Borsani  <https://orcid.org/0000-0002-4140-1367>

#### References

- Accurso, G., Saintonge, A., Catinella, B., et al. 2017, arXiv:1702.03888  
 Aird, J., Nandra, K., Laird, E. S., et al. 2010, *MNRAS*, 401, 2531  
 Alatalo, K., Lisenfeld, U., Lanz, L., et al. 2016, *ApJ*, 827, 106  
 Amorín, R., Muñoz-Tuñón, C., Aguerri, J. A. L., & Planesas, P. 2016, *A&A*, 588, A23  
 Baldry, I. K., Driver, S. P., Loveday, J., et al. 2012, *MNRAS*, 421, 621  
 Baldwin, J. A., Phillips, M. M., & Terlevich, R. 1981, *PASP*, 93, 5  
 Bauermeister, A., Blitz, L., Bolatto, A., et al. 2013, *ApJ*, 763, 64  
 Bell, E. F. 2008, *ApJ*, 682, 355  
 Berta, S., Lutz, D., Nordon, R., et al. 2013, *A&A*, 555, L8  
 Bigiel, F., Leroy, A. K., Jiménez-Donaire, M. J., et al. 2016, *ApJL*, 822, L26  
 Blitz, L., & Rosolowsky, E. 2006, *ApJ*, 650, 933  
 Borthakur, S., Heckman, T., Tumlinson, J., et al. 2015, *ApJ*, 813, 46  
 Boselli, A., Cortese, L., Boquien, M., et al. 2014, *A&A*, 564, A66  
 Boselli, A., Gavazzi, G., Lequeux, J., et al. 1997, *A&A*, 327, 522  
 Bothwell, M. S., Wagg, J., Ciccone, C., et al. 2014, *MNRAS*, 445, 2599  
 Bouché, N., Dekel, A., Genzel, R., et al. 2010, *ApJ*, 718, 1001  
 Boyle, B. J., & Terlevich, R. J. 1998, *MNRAS*, 293, L49  
 Braine, J., & Combes, F. 1992, *A&A*, 264, 433  
 Braine, J., Combes, F., Casoli, F., et al. 1993, *A&AS*, 97, 887  
 Buchbender, C., Kramer, C., Gonzalez-Garcia, M., et al. 2013, *A&A*, 549, A17  
 Carter, M., Lazareff, B., Maier, D., et al. 2012, *A&A*, 538, A89  
 Catinella, B., Haynes, M. P., & Giovanelli, R. 2007, *AJ*, 134, 334  
 Catinella, B., Kauffmann, G., Schiminovich, D., et al. 2012a, *MNRAS*, 420, 1959  
 Catinella, B., Saintonge, A., Janowiecki, S., et al. 2017, *MNRAS*, submitted  
 Catinella, B., Schiminovich, D., Kauffmann, G., et al. 2010, *MNRAS*, 403, 683  
 Catinella, B., Schiminovich, D., Kauffmann, G., et al. 2012b, *A&A*, 544, A65  
 Chabrier, G. 2003, *PASP*, 115, 763  
 Ciccone, C., Bothwell, M., Wagg, J., et al. 2017, arXiv:1705.05851  
 Ciccone, C., Maiolino, R., Sturm, E., et al. 2014, *A&A*, 562, A21  
 Combes, F., García-Burillo, S., Braine, J., et al. 2013, *A&A*, 550, A41  
 Combes, F., Young, L. M., & Bureau, M. 2007, *MNRAS*, 377, 1795  
 Costa, T., Sijacki, D., & Haehnelt, M. G. 2014, *MNRAS*, 444, 2355  
 Crain, R. A., Bahé, Y. M., Lagos, C. d. P., et al. 2017, *MNRAS*, 464, 4204  
 Crain, R. A., Schaye, J., Bower, R. G., et al. 2015, *MNRAS*, 450, 1937  
 Crocker, A., Krips, M., Bureau, M., et al. 2012, *MNRAS*, 421, 1298  
 Daddi, E., Bournaud, F., Walter, F., et al. 2010, *ApJ*, 713, 686  
 Davé, R., Rafieferantsoa, M. H., Thompson, R. J., & Hopkins, P. F. 2017, *MNRAS*, 467, 115  
 Fabello, S., Catinella, B., Giovanelli, R., et al. 2011, *MNRAS*, 411, 993  
 Federrath, C., & Klessen, R. S. 2012, *ApJ*, 761, 156  
 Fumagalli, M., Dessauges-Zavadsky, M., Furniss, A., et al. 2012, *MNRAS*, 424, 2276  
 Gao, Y., & Solomon, P. M. 2004, *ApJ*, 606, 271  
 García-Burillo, S., Combes, F., Hunt, L. K., et al. 2003, *A&A*, 407, 485  
 García-Burillo, S., Usero, A., Alonso-Herrero, A., et al. 2012, *A&A*, 539, A8  
 Geach, J. E., Smail, I., Moran, S. M., et al. 2011, *ApJL*, 730, L19  
 Genel, S., Vogelsberger, M., Springel, V., et al. 2014, *MNRAS*, 445, 175  
 Genzel, R., Tacconi, L. J., Lutz, D., et al. 2015, *ApJ*, 800, 20  
 Geréb, K., Catinella, B., Cortese, L., et al. 2016, *MNRAS*, 462, 382  
 Giovanelli, R., Haynes, M. P., Kent, B. R., et al. 2005, *AJ*, 130, 2598  
 Gnedin, N. Y., & Kravtsov, A. V. 2011, *ApJ*, 728, 88  
 Gonzalez-Perez, V., Lacey, C. G., Baugh, C. M., et al. 2014, *MNRAS*, 439, 264  
 Graciá-Carpio, J., García-Burillo, S., Planesas, P., & Colina, L. 2006, *ApJL*, 640, L135  
 Häring, N., & Rix, H.-W. 2004, *ApJL*, 604, L89  
 Haynes, M. P., Giovanelli, R., Martin, A. M., et al. 2011, *AJ*, 142, 170  
 Helfer, T. T., & Blitz, L. 1993, *ApJ*, 419, 86  
 Hughes, A., Meidt, S., Colombo, D., et al. 2016, in IAU Symp. 315, From Interstellar Clouds to Star-forming Galaxies: Universal Processes?, ed.

- P. Jablonka, P. André, & F. van der Tak (Cambridge: Cambridge Univ. Press), 30
- Hughes, A., Meidt, S. E., Colombo, D., et al. 2013, *ApJ*, 779, 46
- Janowiecki, S., Catinella, B., Cortese, L., et al. 2017, *MNRAS*, 466, 4795
- Kauffmann, G., Heckman, T. M., Tremonti, C., et al. 2003, *MNRAS*, 346, 1055
- Kenney, J. D., & Young, J. S. 1988, *ApJS*, 66, 261
- Kenney, J. D. P., & Young, J. S. 1989, *ApJ*, 344, 171
- Keres, D., Yun, M. S., & Young, J. S. 2003, *ApJ*, 582, 659
- Kewley, L. J., Dopita, M. A., Sutherland, R. S., Heisler, C. A., & Trevena, J. 2001, *ApJ*, 556, 121
- Kewley, L. J., & Ellison, S. L. 2008, *ApJ*, 681, 1183
- Kirkpatrick, A., Pope, A., Aretxaga, I., et al. 2014, *ApJ*, 796, 135
- Koss, M., Mushotzky, R., Veilleux, S., et al. 2011, *ApJ*, 739, 57
- Krips, M., Crocker, A. F., Bureau, M., Combes, F., & Young, L. M. 2010, *MNRAS*, 407, 2261
- Krumholz, M. R. 2013, *MNRAS*, 436, 2747
- Krumholz, M. R., & McKee, C. F. 2005, *ApJ*, 630, 250
- Krumholz, M. R., McKee, C. F., & Tumlinson, J. 2009, *ApJ*, 699, 850
- Lacey, C. G., Baugh, C. M., Frenk, C. S., et al. 2016, *MNRAS*, 462, 3854
- Lagos, C. D. P., Baugh, C. M., Lacey, C. G., et al. 2011, *MNRAS*, 418, 1649
- Lagos, C. d. P., Crain, R. A., Schaye, J., et al. 2015, *MNRAS*, 452, 3815
- Leroy, A. K., Walter, F., Bigiel, F., et al. 2009, *AJ*, 137, 4670
- Leroy, A. K., Walter, F., Brinks, E., et al. 2008, *AJ*, 136, 2782
- Leroy, A. K., Walter, F., Sandstrom, K., et al. 2013, *AJ*, 146, 19
- Lilly, S. J., Carollo, C. M., Pipino, A., Renzini, A., & Peng, Y. 2013, *ApJ*, 772, 119
- Lisenfeld, U., Espada, D., Verdes-Montenegro, L., et al. 2011, *A&A*, 534, A102
- Magdis, G. E., Daddi, E., Sargent, M., et al. 2012, *ApJL*, 758, L9
- Magnelli, B., Saintonge, A., Lutz, D., et al. 2012, *A&A*, 548, A22
- Magorrian, J., Tremaine, S., Richstone, D., et al. 1998, *AJ*, 115, 2285
- Martindale, H., Thomas, P. A., Henriques, B. M., & Loveday, J. 2016, arXiv:1606.08440
- McAlpine, S., Helly, J. C., Schaller, M., et al. 2016, *A&C*, 15, 72
- Merloni, A., Bongiorno, A., Bolzonella, M., et al. 2010, *ApJ*, 708, 137
- Merloni, A., & Heinz, S. 2013, in *Evolution of Active Galactic Nuclei*, ed. T. D. Oswalt & W. C. Keel (Dordrecht: Springer), 503
- Obreschkow, D., & Rawlings, S. 2009, *MNRAS*, 394, 1857
- Pettini, M., & Pagel, B. E. J. 2004, *MNRAS*, 348, L59
- Popping, G., Behroozi, P. S., & Peeples, M. S. 2015, *MNRAS*, 449, 477
- Popping, G., Somerville, R. S., & Trager, S. C. 2014, *MNRAS*, 442, 2398
- Radford, S. J. E., Downes, D., & Solomon, P. M. 1991, *ApJL*, 368, L15
- Rosolowsky, E., Leroy, A. K., Usero, A., et al. 2015, in *American Astronomical Society Meeting Abstracts* 225, 141.25
- Sage, L. J. 1993, *A&A*, 272, 123
- Saintonge, A., Catinella, B., Cortese, L., et al. 2016, *MNRAS*, 462, 1749
- Saintonge, A., Kauffmann, G., Kramer, C., et al. 2011a, *MNRAS*, 415, 32
- Saintonge, A., Kauffmann, G., Wang, J., et al. 2011b, *MNRAS*, 415, 61
- Saintonge, A., Tacconi, L. J., Fabello, S., et al. 2012, *ApJ*, 758, 73
- Saito, T., Iono, D., Xu, C. K., et al. 2017, *ApJ*, 835, 174
- Sakamoto, K., Okumura, S. K., Ishizuki, S., & Scoville, N. Z. 1999, *ApJ*, 525, 691
- Sakamoto, S., Hasegawa, T., Hayashi, M., Handa, T., & Oka, T. 1995, *ApJS*, 100, 125
- Sanders, D. B., & Mirabel, I. F. 1985, *ApJL*, 298, L31
- Seko, A., Ohta, K., Yabe, K., et al. 2016, *ApJ*, 819, 82
- Schaye, J., Crain, R. A., Bower, R. G., et al. 2015, *MNRAS*, 446, 521
- Schechter, P. 1976, *ApJ*, 203, 297
- Schiminovich, D., Catinella, B., Kauffmann, G., et al. 2010, *MNRAS*, 408, 919
- Serra, P., Oosterloo, T., Morganti, R., et al. 2011, arXiv:1111.4241
- Serra, P., Oser, L., Krajinović, D., et al. 2014, *MNRAS*, 444, 3388
- Shimizu, T. T., Mushotzky, R. F., Meléndez, M., Koss, M., & Rosario, D. J. 2015, *MNRAS*, 452, 1841
- Solomon, P. M., Downes, D., Radford, S. J. E., & Barrett, J. W. 1997, *ApJ*, 478, 144
- Somerville, R. S., Hopkins, P. F., Cox, T. J., Robertson, B. E., & Hernquist, L. 2008, *MNRAS*, 391, 481
- Springob, C. M., Haynes, M. P., Giovanelli, R., & Kent, B. R. 2005, *ApJS*, 160, 149
- Springob, C. M., Masters, K. L., Haynes, M. P., Giovanelli, R., & Marinoni, C. 2007, *ApJS*, 172, 599
- Stanway, E. R., Levan, A. J., Tanvir, N. R., Wiersema, K., & van der Laan, T. P. R. 2015, *ApJL*, 798, L7
- Sturm, E., González-Alfonso, E., Veilleux, S., et al. 2011, *ApJL*, 733, L16
- Tacconi, L. J., Genzel, R., Neri, R., et al. 2010, *Natur*, 463, 781
- Tacconi, L. J., Genzel, R., Saintonge, A., et al. 2017, arXiv:1702.01140
- Tacconi, L. J., Neri, R., Genzel, R., et al. 2013, *ApJ*, 768, 74
- Tiley, A. L., Bureau, M., Saintonge, A., et al. 2016, *MNRAS*, 461, 3494
- Troncoso, P., Maiolino, R., Sommariva, V., et al. 2014, *A&A*, 563, A58
- Ueda, J., Iono, D., Petitpas, G., et al. 2012, *ApJ*, 745, 65
- Usero, A., Leroy, A. K., Walter, F., et al. 2015, *AJ*, 150, 115
- Vallini, L., Gruppioni, C., Pozzi, F., Vignali, C., & Zamorani, G. 2016, *MNRAS Letters*, 456, L40
- Wang, J., Overzier, R., Kauffmann, G., von der Linden, A., & Kong, X. 2010, *MNRAS*, 401, 433
- Weinmann, S. M., Kauffmann, G., van den Bosch, F. C., et al. 2009, *MNRAS*, 394, 1213
- Wu, J., Evans, N. J., II, Gao, Y., et al. 2005, *ApJL*, 635, L173
- Wyder, T. K., Martin, D. C., Schiminovich, D., et al. 2007, *ApJS*, 173, 293
- Yesuf, H. M., French, K. D., Faber, S. M., & Koo, D. C. 2017, arXiv:1705.00668
- Young, J. S., Xie, S., Tacconi, L., et al. 1995, *ApJS*, 98, 219
- Young, L. M., Bureau, M., Davis, T. A., et al. 2011, *MNRAS*, 414, 940